December 1999 • NREL/SR-520-27666

Subcontractor Report

High Efficiency Thin Film CdTe and a-Si Based Solar Cells

Annual Technical Report
March 4, 1998 — March 3, 1999

A.D. Compaan, X. Deng, and R.G. Bohn
Department of Physics and Astronomy
The University of Toledo
Toledo, Ohio

National Renewable Energy Laboratory

1617 Cole Boulevard
Golden, Colorado 80401-3393

NREL is a U.S. Department of Energy Laboratory
Operated by Midwest Research Institute • Battelle • Bechtel

Contract No. DE-AC36-99-GO10337

December 1999 • NREL/SR-520-27666

High Efficiency Thin Film CdTe and a-Si Based Solar Cells

Annual Technical Report
March 4, 1998 — March 3, 1999

A.D. Compaan, X. Deng, and R.G. Bohn
Department of Physics and Astronomy
The University of Toledo
Toledo, Ohio

NREL Technical Monitor: B. von Roedern

Prepared under Subcontract No. ZAF-8-17619-14

National Renewable Energy Laboratory

1617 Cole Boulevard
Golden, Colorado 80401-3393

NREL is a U.S. Department of Energy Laboratory
Operated by Midwest Research Institute • Battelle • Bechtel

Contract No. DE-AC36-99-GO10337

NOTICE

Available electronically at http://www.doe.gov/bridge

Available for a processing fee to U.S. Department of Energy
and its contractors, in paper, from:

U.S. Department of Energy
Office of Scientific and Technical Information
P.O. Box 62
Oak Ridge, TN 37831-0062
phone: 865.576.8401
fax: 865.576.5728
email: reports@adonis.osti.gov

Available for sale to the public, in paper, from:

U.S. Department of Commerce
National Technical Information Service
5285 Port Royal Road
Springfield, VA 22161
phone: 800.553.6847
fax: 703.605.6900
email: orders@ntis.fedworld.gov
online ordering: http://www.ntis.gov/ordering.htm

Printed on paper containing at least 50% wastepaper, including 20% postconsumer waste

SUMMARY

This report covers the first year of this subcontract for research on high efficiency CdTe-based thin-film solar cells and on high efficiency a-Si-based thin-film solar cells. The effort on CdTe-based materials is led by Prof. Compaan and emphasizes the use of sputter deposition of the semiconductor layers. The effort on high efficiency a-Si materials is led by Prof. Deng and emphasizes plasma-enhanced chemical vapor deposition for cell fabrication with major efforts on triple-junction devices.

Major accomplishments for the CdTe group over the past year include the following:

- We have constructed a second dual magnetron sputter deposition facility.
- We have optimized reactive sputtering for ZnTe:N films to achieve 10 Ω-cm resistivity and ~9% efficiency cells with a copper-free ZnTe:N/Ni contact.
- We identified Cu-related photoluminescence features and studied their correlation with cell performance including their dependence on temperature and E-fields.
- We studied band-tail absorption in CdS_xTe_{1-x} films at 10 K and 300 K,
- We collaborated with the National CdTe PV Team on 1) studies of high resistivity tin oxide layers from ITN Energy Systems, 2) fabrication of cells on the HRT layers with 0, 300, & 800 nm CdS, and 3) preparation of ZnTe:N-based contacts on First Solar materials for stress testing.
- We collaborated with 1) Brooklyn College for ellipsometry studies of CdS_xTe_{1-x} alloy films, and 2) the U. of Buffalo/Brookhaven NSLS for synchrotron x-ray fluorescence studies of interdiffusion in CdS/CdTe bilayers.

Over the past year the a-Si group has worked on the following three task areas: 1) optimization of triple-junction a-Si solar cells; 2) development of novel processes for high quality a-SiGe deposition; and 3) improvement in device designs. Particular emphasis was put on the optimization of triple-junction solar cells. Highlights of our progress in the first year:

- We have established a base line for the fabrication of a-Si based solar cells with single, tandem and triple junction structures.
- We have achieved the fabrication of a-Si/a-SiGe/a-SiGe triple-junction solar cells with an initial efficiency of 9.7% during the second quarter, and 10.6% during the fourth quarter.
- After 1166 hours of light soaking under 1 sun light intensity at 50 ^{o}C, these 10.6% solar cells have stabilized at approximately 9%.
- We have fabricated wide bandgap a-Si top cells. The highest V_{oc} achieved for our single-junction top cell was 1.02 V. Top cells with high FF (up to 74%) were fabricated routinely.
- High quality narrow bandgap a-SiGe solar cells with 8.3% efficiency were fabricated.
- Bandgap graded buffer layers were found to improve the performance (V_{oc} and FF) of the narrow bandgap a-SiGe bottom cells.
- We studied the sputter deposition of ITO films for the top electrode on a-Si cells and found that a small amount of oxygen partial pressure (~2×10^{-5} Torr) was beneficial for growing high quality films from ITO targets.
- The a-Si group has collaborated with various team members including ECD, United Solar, Univ. of North Carolina, UCLA and SUNY-Buffalo.

The a-Si:H group and the CdTe group share many instrumentation resources at UT. During this year, our instrumentation infrastructure was significantly enhanced with funding from NREL matched by the UT President's Fund. We have acquired, or will be acquiring, a Dektak^3 profilometer, solar simulator, VHF power amplifier, mass flow controllers, a tunable diode laser, and a variety of vacuum and spectroscopic equipment.

TABLE OF CONTENTS

LIST OF FIGURES

LIST OF TABLES

1 Introduction

1.1 Background

This annual report covers the first year of an NREL subcontract with the University of Toledo which supports cell fabrication and related materials studies on two types of thin-film solar cells, CdTe-based and a-Si:H-based.

1.2 Technical Approach

1.2.1 Cadmium Telluride-Based Cells

Magnetron sputtering— Our CdTe-based effort is focused on the use of rf sputtering for thin film deposition. Much of our effort is designed to exploit the effects of excited state species in the plasma to improve the film growth or lower the growth temperature. The ultimate goal is to fabricate rf sputtered CdS/CdTe thin film solar cells with efficiencies exceeding 15% on soda-lime glass. For the CdS and CdTe deposition, we utilize a specially designed two-gun magnetron sputtering chamber with optical thickness monitors as described previously. During the past year we have constructed a second, similar sputtering chamber which is used for deposition of contact structures. In this chamber we have done reactive sputtering of ZnTe:N. This is one example of utilizing the energy in the sputtering plasma, in this case to dissociate N_2 to make atomic N available for electrically-active incorporation in the film. A third sputtering system has been used, this year, to extend the range of metals available for contact structures. This dc magnetron sputtering system has been used for the deposition of Ni on top of the ZnTe:N layers.

Pulsed Laser Deposition--We have continued to make limited use of PLD as a convenient method for preparation of films with unusual composition. Thus, during the past year we have prepared additional films of the ternary alloy CdS_xTe_{1-x} and thin bilayers of CdS/CdTe for experiments with collaborators at Brooklyn College and the Univ. of Buffalo.

Post-Deposition Processing—For post-deposition processing of the sputtered films we have now standardized on a vapor $CdCl_2$ treatment and can handle substrate sizes of about three-inch square.

1.2.2 Amorphous-Silicon-Based Cells

Triple-cell fabrication—One of our focused efforts is to fabricate high efficiency triple-junction a-Si based solar cells. PECVD process is used for the deposition of all semiconductor layers. This study includes the optimization of a-Si and a-SiGe intrinsic layers with improved network ordering, optimization of doped microcrystalline silicon p-layers and amorphous silicon n-layers, optimization of tunnel junctions and interfaces. The goal is to achieve 12.5% stable solar cells (total area) at the end of Year 3.

Novel processes for high quality narrow-bandgap a-SiGe deposition—Various approaches are used to explore the deposition of narrower-bandgap (~1.3 eV) a-SiGe materials. A multi-layer approach having alternating layers of a-Si and a-Ge is being studied. A hot-wire chamber is being constructed for high-rate and high quality a-SiGe deposition.

Non-semiconductor layers—We also optimize the deposition of ITO and other non-semiconductor layers which are required for the solar cell operation. Interfaces between semiconductor and the non-semiconductor layers, ITO top electrodes and ZnO back-reflector, are being explored.

1.2.3 Characterization Tools

For characterization of films and cells, we continue to use SEM, EDS, x-ray, Raman, photoluminescence, optical absorption, Hall measurements, C-V, I-V, and SQE. We have continued collaborative efforts with Case Western Reserve University for Rutherford Backscattering and XPS measurements, electroluminescence measurements with the University of North Carolina, mobility-lifetime measurements with UCLA, and synchrotron x-ray measurements with the University of Buffalo and Brookhaven National Lab, and ellipsometry with Brooklyn College (CUNY).

2 CdTe-Based Materials and Cells

In this section we shall discuss progress and results on the following projects: 1) the vapor $CdCl_2$-treatment system, 2) first results on reactively sputtered ZnTe:N films and contacts, 3) photoluminescence studies of the movement of Cu in CdTe crystals and thin-film cells, 4) XPS studies of CdTe film surfaces, 5) consumption of CdS during vapor $CdCl_2$ processing, 6) studies of cell performance vs. CdTe thickness, 7) absorption measurements on CdS_xTe_{1-x} alloys at 10 K and 300 K, 8) teaming activities, and 9) other collaborative activities.

2.1 Evolution of the vapor $CdCl_2$-treatment process

For the period covered by this report we have used a vapor $CdCl_2$-treatment process for the post-deposition treatment of our cells.[2.1] Our system is scaled to accept three-inch glass substrates, with halogen lamp heating of SiC_6-coated graphite blocks. Graduate student Konstantin Makhratchev has performed a study to optimize empirically the heating parameters for best cell performance. He has found that more reproducible cell performance is obtained with quite small amounts of $CdCl_2$ in the graphite receptacle. Thus we currently use a charge of 2 ml of saturated $CdCl_2$/methanol dropped into the warm bottom graphite receptacle. Such a charge lasts for about 25 runs. Furthermore, we have found that good results are obtained with very low flow of dry air. Too much air flow leads to nonuniform heating of the cell and cool spots at the cell edges. Thus we currently use an airflow duty cycle, flow on to flow off of 1/15 with the flow rate on of 30 sccm. In addition, we find somewhat better results with the cell more tightly enclosed over the $CdCl_2$ reservoir. The upper graphite block, in contact with the glass side of the cell is kept at ~387 ^oC and the lower block containing the reservoir of $CdCl_2$ is also kept at ~387^oC. In order to maintain consistency in the temperature ramp-up procedure and annealing time and reduce labor by the operator, we designed an interface that allows the furnace heaters and gas solenoid to be controlled by computer. Typical annealing parameters are: ramp up time approximately 25 min, hold time 30 min and cool down time approximately 30 min.

2.2 Studies of ZnTe:N for back contact applications

This effort on the reactive sputter deposition of doped ZnTe is directed toward the development of a material which would facilitate a low resistance back contact to CdTe without creating the sort of problems which can arise with the commonly used copper in the back contact material.

2.2.1 Construction of new sputtering chamber

Finding a good, low resistance back contact to the CdS/CdTe solar cells is a high priority. The back contact is believed to affect not only the efficiency but also the stability of solar cells. Cu/Au, ZnTe:Cu/Au, ZnTe:Cu/Ni, and graphite paste doped with HgTe:Cu are the commonly used contact schemes. Copper is present in all of these back-contact schemes. At the same time copper is believed to play an important role in the deterioration of the efficiency. In order to develop a copper-free back contact, we started some research on ZnTe:N films during the 1992-1994 period. ZnTe:N films with resistivity of 17 Ω-cm were obtained[2.2]. However, in those

studies we did not obtain good performance of this material as a back contact.

We resumed our research on ZnTe:N films using a reactive sputtering process in January 1998. To allow the exploration of the novel contact structure without disrupting our standard cell fabrication procedure, graduate student, Xianda Ma constructed a new rf-magnetron sputtering system from an existing spare vacuum chamber and used it for ZnTe depositions. His work is detailed in his M.S. thesis.[2.3] Highlights are provided below. The main features of this system are: The system has two 2-inch planar magnetrons, constructed in house. The base pressure is 4.3×10^{-7} Torr. Two independent incoming gases can be used in the sputtering process. The controllable sputtering pressure is from 1 mTorr to 1 Torr.

2.2.2 ZnTe:N films on Corning 7059 glass

We first explored the growth parameters for the ZnTe:N films to find optimum conditions for growing low-resistivity ZnTe:N. Varied parameters were substrate temperature, total incoming gas flow rate, and nitrogen/argon ratio in the incoming gas flow. We found the lowest resistivity (~5 Ω-cm) films were fabricated with a substrate temperature of 360 ^{o}C, total incoming gas flow rate of 71.5 sccm, and nitrogen/(argon+nitrogen) ratio of the inlet gas of 1.25-2.5%. Figure 2.2.1 presents the resistivity vs. the ratio of nitrogen gas for a series of films grown at 360 ^{o}C, 71.5 sccm of total flow rate, 90 minutes of deposition time at 30 watts of RF power, and 20 mTorr of deposition pressure. We were unable to determine conclusively by Hall measurements the carrier type and carrier concentration due to the low mobility of the films, but hot probe tests show the material to be p-type.

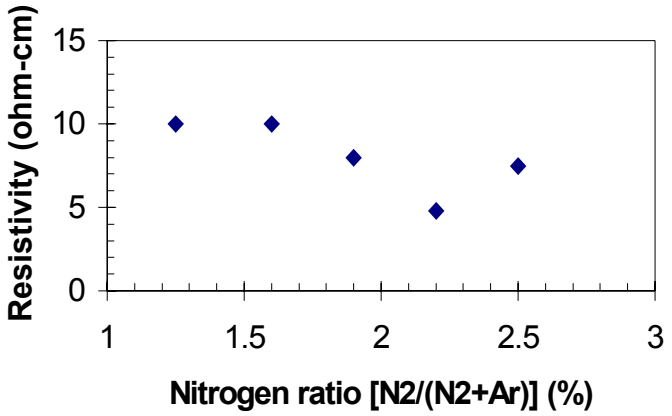

Figure 2.2.1 Resistivity vs. $N_2/(N_2+Ar)$ ratio, at substrate temperature: 360 ^{o}C, deposition time: 90 minutes, total flow rate: 71.5 sccm

2.2.3 ZnTe:N films as a contact buffer layer in CdS/CdTe solar cells

After optimizing the growth conditions for low-resistivity ZnTe:N films on the 7059 borosilicate glass, we fabricated copper-free back contacts using ZnTe:N films on three types of CdS/CdTe cells: UT all-sputtered cells, First Solar wet-$CdCl_2$ treated cells, and First Solar vapor-$CdCl_2$ treated cells. For the initial stages of the ZnTe study, we focused on optimizing the

ZnTe:N contacts on First Solar wet-$CdCl_2$ treated cells ("wet" refers to a methanol/$CdCl_2$ solution) in order to participate in the stability teaming activity. (See Section 2.8.1) Several contact schemes involving nitrogen-doped ZnTe and/or nominally intrinsic ZnTe were used, including metal/ZnTe:N/CdTe/CdS, metal/ZnTe:N/ZnTe/ CdTe/CdS, and metal/ZnTe/CdTe/CdS. Metals used were Ni, Au, and Cu/Au. Cu and Au contacts were deposited with thermal evaporation, and Ni contacts were deposited using the triple-gun Varian DC sputtering system recently acquired by our laboratory.

Table 2.2.1 shows the comparison between some cells made from First Solar wet-$CdCl_2$ treated cells. The maximum efficiency we have obtained thus far is 10.8% (measured in our own I-V system) for cell 3, with a ZnTe/ZnTe:N/Ni back contact. (Note that due to a calibration error in our I-V system, we believe the efficiencies for cells 3 and 4 to be about 1% too high.) Note also that the copper-free ZnTe/ZnTe:N/Ni contact scheme is at least as good as the ZnTe/Cu/Au contact. We have also grown cells with only ZnTe:N/metal (with no intrinsic ZnTe buffer layer) and obtained similar efficiencies. Further work is under way to improve the fill factor and the open circuit voltage and understand the role of the N doping of the ZnTe contact.

The best of these copper-free contacted cells were delivered to First Solar for stress measurements. After one month of storing similar cells in the laboratory at room temperature we re-measured several cells with ZnTe/ZnTe:N/Ni, ZnTe/ZnTe:N/Au and Cu/Au contact schemes. No special stress testing conditions were used. Table 2.2.2 shows that the ZnTe/ZnTe:N/Ni contact scheme is stable under these conditions, although we have begun to observe some reduced performance under stressing. These results show there is some potential for Cu-free back contacts based on ZnTe:N.

Table 2.2.1 Comparison of the performance of cells with different contact schemes

Cell #	1	2	3	4
Contact scheme	ZnTe/Cu/Au	ZnTe/Au	ZnTe/ZnTe:N/Ni	ZnTe/ZnTe:N/Au
Voc(V)	0.796	0.772	0.741	0.748
Jsc(mA/cm^2)	17.5	20.2	23.2	21.1
Fill Factor(%)	62.43	56.50	62.96	62.79
Efficiency(%)	8.7	8.8	10.8	9.9
ZnTe thickness (nm)	186	186	27.9	27.9
ZnTe:N thickness (nm)	0	0	158.1	158.1
Total flow rate(sccm)	40	40	71.5	71.5
Nitrogen ratio(%)	0	0	1.9	1.9
Heating power(W)	155.8	155	155.4	155.4
Diffusion Temp.(C)	225	150	206	175
Diffusion Time(min)	45	45	45	45

Table 2.2.2 Preliminary stability results for different contact schemes after 35 or 42 days

Contact	ZnTe/ZnTe:N/Au		ZnTe/ZnTe:N/Ni		Cu/Au	
	Original	35 days	Original	42 days	Original	35 days
Efficiency(%)	9.9	7.9	10.1	10.1	10.3	9.1
Voc(V)	0.748	0.740	0.750	0.762	0.787	0.779
Jsc($mA/cm)^2$)	21.1	19.7	23.7	23.1	19.9	19.8
Fill Factor(%)	62.79	54.48	56.9	57.4	65.85	58.9

In contrast with the promising results obtained with the wet-treated First Solar CdTe material, we have not achieved over 6% efficiency with either UT all-sputtered-CdS/CdTe cells or First Solar vapor-$CdCl_2$ treated CdS/CdTe cells using the copper-free, ZnTe contact scheme. However, we have obtained efficiencies up to 8% on First Solar CdTe which was vapor $CdCl_2$-treated in our lab. We believe the lower growth temperature the UT cells may result in a different optimum ZnTe growth temperature for the two cell types. Furthermore, the contacting process may be sensitive to residual Cl at the surface. It should be noted that no chemical etching was used prior to the contacting so we do not expect a Te-rich surface layer but oxides are almost certainly present. (See Section 3.4 below.) We are presently working to optimize further the sputtered ZnTe:N contact process.

2.3 Cu migration in CdS/CdTe solar cells

There is accumulating evidence that the use of copper in the back contact to CdTe can lead to deterioration in the performance of CdTe-based solar cells. However, the detailed nature of the role of copper and how it acts to provide better ohmic contact is not very clear. Furthermore, it is not completely clear how Cu moves in the polycrystalline CdTe films and what energy levels and lattice positions are involved. We have begun a series of studies, using mainly photoluminescence, to try to help clarify some of these issues.

Graduate student Dan Grecu has used photoluminescence (PL) from 10 K to 300 K to study Cu migration in CdS/CdTe solar cells both as a result of thermally activated diffusion and under the influence of an externally applied electric field. In the sections below we show the luminescence from *single crystal* CdTe and identify changes related to thermally diffused Cu. We then study Cu thermal diffusion in *polycrystalline* CdTe in solar cell device structures, collecting luminescence from the CdS junction region, and observe changes similar to the single crystal case. Finally, we apply electric fields of different polarity across the CdS/CdTe junction to study Cu electromigration. We observe dramatic changes in the PL upon application of an electric field consistent with Cu diffusing interstitially as Cu^+.

PL spectra typically were recorded at 10K. The excitation was achieved with the 752.5nm line of a Kr laser focused on the sample with a spot size of 0.2-0.5 mm and operating with powers ranging between 20mW to 0.02mW. At this wavelength the absorption depth is approximately 0.3μm. Note that 0.1 mW focused to a $(0.3\ mm)^2$ spot is about 100 mW/cm^2 or one sun.

2.3.1 Cu in single crystal CdTe

For the single-crystal study, the entire CdTe crystal was first etched for 30s in 1% Br:MeOH. Then 10nm of Cu was deposited on part of the CdTe by thermal evaporation. Following deposition the crystal was annealed in air at 150°C for 60 minutes.

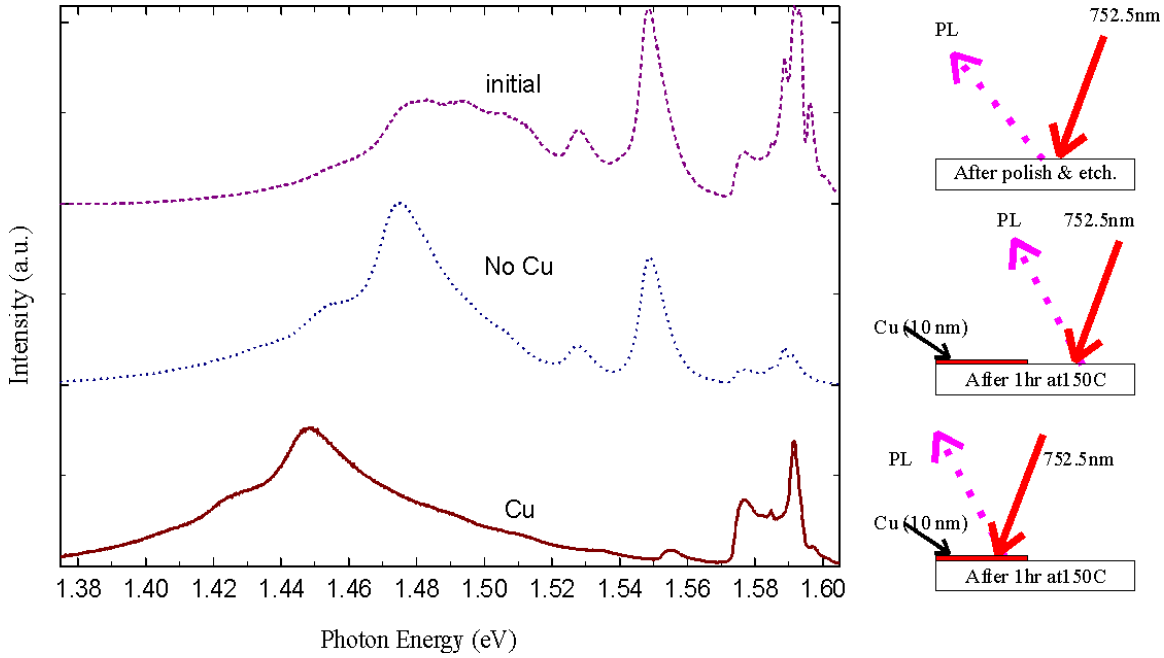

Figure 2.3.1 Spectra of single crystal CdTe initially and after 1hr. anneal at 150 ^{o}C in air. All spectra recorded at 10K with 2mW excitation power.

The effects of Cu migration on the PL spectra are shown in Figure 2.3.1. Immediately after etch the spectrum labeled "initial" consists of a cluster of bound exciton transitions in the region 1.58-1.60eV, a strong donor-acceptor pair (DAP) transition at 1.55eV and its phonon replica at 1.52eV, and a broad "defect" band ranging approximately from 1.40 to 1.52eV consisting of several donor- deep acceptor state transitions and phonon replicas.

Immediately after Cu evaporation on part of the crystal, the spectra from the regions with and without deposited Cu (not shown) are similar with a slightly reduced intensity for the part of the sample with Cu. After annealing at 150°C, PL from the regions with and without Cu is markedly different (curves "Cu" and "No Cu" in Figure 2.3.1). While both parts of the sample show decreased excitonic transitions relative to the "defect" band, the excitonic region of the sample diffused with Cu is dominated by the transition at 1.59eV. For this sample the transition at 1.55eV is strongly attenuated and a new strong "defect" transition emerges at 1.45eV.

The quenching of the 1.55eV DAP feature can be explained if a Cd vacancy is the acceptor in this transition ([2.4] and references therein) and Cu^{+} -V_{Cd} complexes and/or Cu_{Cd} states are formed. The 1.45 eV transition and a bound exciton at 1.5896eV (consistent with our peak at 1.59eV) were previously attributed to Cu_{Cd}[2.5].

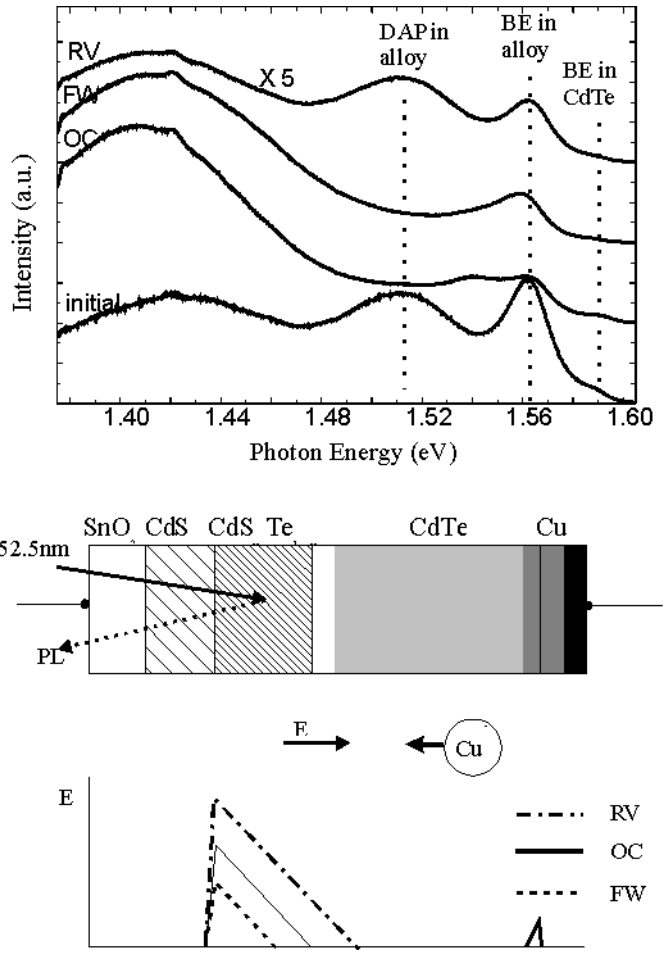

Figure 2.3.2. PL spectra from First Solar films annealed for 70 hours at 150 ^{o}C under different electrical bias conditions. Spectra taken at 10K using 2mW excitation power at 752 nm. The two sketches illustrate the device structure and built-in fields assuming heavily doped n^{+}-CdS and a heavily doped p^{+}-layer at the back contact.

2.3.2 Cu in CdTe/CdS solar cell structures

The solar cells used in the study were deposited on commercial glass/SnO_2 substrates by vapor transport deposition at First Solar, LLC. and have approximately 0.3μm CdS and 4μm CdTe. All the samples were wet $CdCl_2$ treated and have grains of approximately 2μm in diameter. To observe the effects of Cu diffusion, the First Solar samples were deposited with layers of Cu between 1 and 10 nm thick using radio-frequency (rf) sputtering. (The 1 to 10 nm thick layer behaved as an infinite source for diffusion. The amount of initial copper had no observed effect on the PL.) The samples underwent different annealing steps and the PL spectra were recorded after each of these steps. In addition we included two of our rf-deposited samples, one which had an undoped CdTe layer and one which was co-sputtered with 2% Cu as determined by Inductively Coupled Plasma Spectroscopy (ICPS) and Energy Dispersive x-ray Spectroscopy (EDS).

The PL spectrum from the CdS/CdTe junction of a First Solar cell, in Figure 2.3.3 curve "initial", is consistent with the formation of a $CdS_{0.05}Te_{0.95}$ alloy region with smaller bandgap.

This can be easily seen from the 30 meV shift in both the excitonic transition (1.59→1.56eV) and the DAP (1.55→1.52eV). A broad band centered at 1.42eV is also observed analogous to the 1.45eV band in the single crystal material.

After 180 minutes of diffusion with Cu at 250°C the spectrum (not shown) is similar to curve "FW" in Figure 2.3.2 showing the quenching of the 1.52eV transition and an increase in the broad-band intensity. In contrast to this, samples that did not have Cu maintained the original PL features. The 1.52eV band can be detected in rf sputtered samples with nominally no Cu but not in those with 2% Cu content. Anneals at *lower temperatures* show considerably less reduction of the PL intensity of this transition.

Identification of the various features in the PL spectrum can be challenging. However, several characteristics can be used to identify donor-acceptor pair (DAP) lines. DAP luminescence line energies depend on the pair separation in the lattice so that they give rise to a characteristic spectrum of lines or asymmetric bands. Furthermore, because of their limited number, their intensity dependence is generally sublinear in excitation power whereas exciton-related lines are superlinear, since they are due to the recombination of two photo-induced particles. We have verified this intensity dependence for the DAP line at 1.55 eV in crystalline CdTe and at 1.52 eV in the tellurium-rich polycrystalline alloy. In addition, the intensity dependence on temperature can yield the characteristic binding energies of the donor and acceptor states. The normalized intensity dependence of the DAP transition in crystalline CdTe at 1.55 eV (10K) is shown in the left panel of Fig. 2.3.3 for the temperature range of 10K to 100 K. Similarly the intensity dependence of the DAP transition at 1.52 eV in the polycrystalline alloy of a solar cell structure is shown in the right panel for the temperature range of 20K to 100K. (Although the DAP transition at 1.55 eV in the single crystal CdTe (see Fig. 2.3.1) is narrower than the DAP transition at 1.52 eV in the polycrystalline alloy (Fig. 2.3.2), the peak intensities have similar orders of magnitude.) The dotted lines are fits to the DAP intensity with the following functional form:

$$I = I_o \{[1-\exp(-E_1/kT)][1-\exp(-E_2/kT)]\},$$

where E_1 and E_2 are the ionization energies of the electron from the donor level and the hole from the acceptor level. For crystalline CdTe, we find the two energies are 5.6 ±0.5 meV and 51 ±8 meV. For the alloy, the two energies are less certain because the peak is broader, but we obtain 5±3 meV and 41±7 meV. Donors in CdTe are typically hydrogenic with a binding energy of about 5 to 6 meV, so we identify the larger binding energy as that of the acceptor state and this energy has been identified typically as a state of the Cd vacancy (V_{Cd}). Thus the disappearance of this DAP emission line when Cu is introduced (Figs. 2.3.1 and 2.3.3) is consistent with this assignment. That is, the V_{Cd} donor is annihilated when Cu occupies the Cd site to produce Cu_{Cd}. Furthermore, the broad peak near 1.45 eV in Cu-doped CdTe may be a deeper DAP peak arising from a donor and the Cu_{Cd} acceptor.

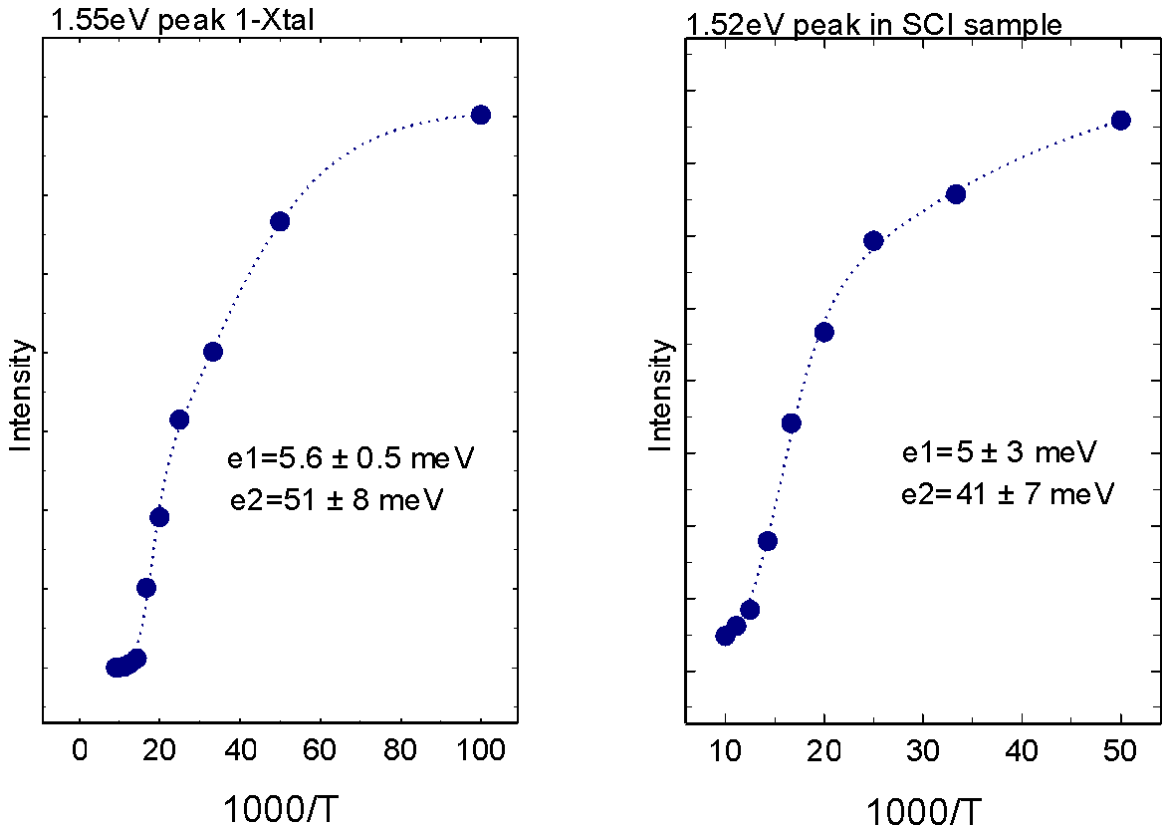

Fig. 2.3.3. Intensity of the DAP lines in crystalline CdTe (left panel) and in alloyed region of a First Solar CdS/CdTe structure vs. temperature. Excitation at 1.648 eV.

2.3.3 Electromigration studies

For the study of electromigration, samples were prepared similarly with the addition of metal contacts as a final layer and annealed using an external electrical bias applied between the metal layer and the SnO_2.

In Figure 2.3.3, showing samples annealed with the simultaneous application of an external electric field, it is observed that Cu diffusion leads to the disappearance of the 1.52eV band in the cases of the open circuit (OC) and forward bias (FW) of +1V but not in the case of a -1V reverse bias (RV). This result is consistent with Cu diffusing as a positively charged ion. The built-in field of the depletion region slows the concentration-gradient-driven diffusion of Cu^+ towards the junction. Following diffusion, Cu^+ is likely to form complexes with V_{Cd} and/or Cu_{Cd} acceptor states leading to the observed quenching of the 1.52eV transition and reported increase in V_{oc} of the devices[2.6] by p doping of the CdTe layer, especially near the back contact.

Interpretation of the changes in the "defect" band around 1.42eV as well as in the excitonic region is complicated by the polycrystalline nature of the material that leads to broader spectral features. The relative increase of the 1.52eV band with respect to the excitonic transitions in the case of the forward and open-circuit conditions support our interpretation that Cu_{Cd} acceptors are formed.

Changes in the PL can be partially reversed using an appropriate electric field. An example is given in Figure 2.3.4 which shows the PL spectra of a sample that was annealed under open-

circuit conditions for 70 minutes followed by reverse-bias (-1V) for 40 hours. The results show that Cu^{+}-V_{Cd} complexes or $Cu_{Cd} \rightarrow V_{Cd}$ states are dissociated in the increased electric field in the depletion region and the original DAP line at 1.52eV is partially recovered.

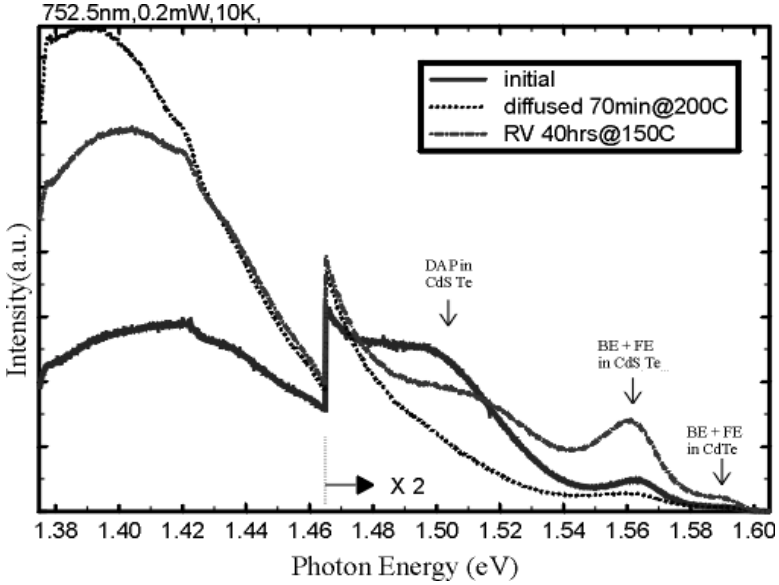

Figure 2.3.4. The effect of an applied reverse bias on the junction PL. Spectra recorded at 10K with 0.2 mW at 752 nm. CdS/CdTe films from First Solar.

In summary we identified changes in the PL spectrum of CdTe associated with the diffusion of Cu. We showed that the DAP transition at 1.52eV, associated with Cd vacancies, is quenched by the diffusion of Cu consistent with the formation of Cu^{+}-V_{Cd} complexes and/or Cu_{Cd} states. The application of an electric field strongly influences Cu migration and the formation/dissociation of the Cu^{+}-V_{Cd} / Cu_{Cd} states and will affect the solar cell electrical properties by modifying the doping profile and carrier concentration in the CdTe layer.[2.7] Observed changes in performance of cells with and without Cu, under various stress conditions, are now being correlated with these changes in PL to begin to identify the mechanisms involved. This will be a major focus in the next phase.

2.4 XPS measurements on $CdCl_2$-treated CdTe: wet vs. vapor treatments

In Section 2.2 above, we described substantial differences between the performance of ZnTe-based contacts on CdTe surfaces which were vapor treated and those which were wet-treated with $CdCl_2$. Partly because of this experience, Dan Grecu performed an x-ray photoelectron spectroscopy (XPS) investigation at Case Western University of CdS/CdTe bilayers with the goal of understanding the surface changes that occur during the $CdCl_2$ treatment. A set of samples were prepared by rf sputtering with nominal thickness of 200nm CdS and 200nm CdTe on a quartz substrate. The samples were $CdCl_2$ annealed using the vapor transport process at 340, 360, 380 and 400 °C.

The annealed samples were studied directly without any surface preparation. To quantify the amount of oxidation on the surface we used the Te $3d_{5/2}$ peak. The peak corresponding to Te

in TeO_2 (or perhaps other compounds involving both oxygen and chlorine [2.8]) is chemically shifted to higher binding energies by about 3.66 eV from the Te peak due to CdTe [2.9].

Fig.2.4.1 shows the Te $3d_{5/2}$ and $3d_{3/2}$ photoelectron peaks. The ratio of the amplitude of the $3d_{5/2}$ peak due to TeO_2 to the sum of the amplitudes of the two $3d_{5/2}$ peaks is a quantitative measure of the surface oxidation as shown in the figure inset. It can be observed from the figure that an increased oxidation occurs for temperatures around 400°C, which is a typical temperature for $CdCl_2$ treatments commonly employed for solar cells devices.

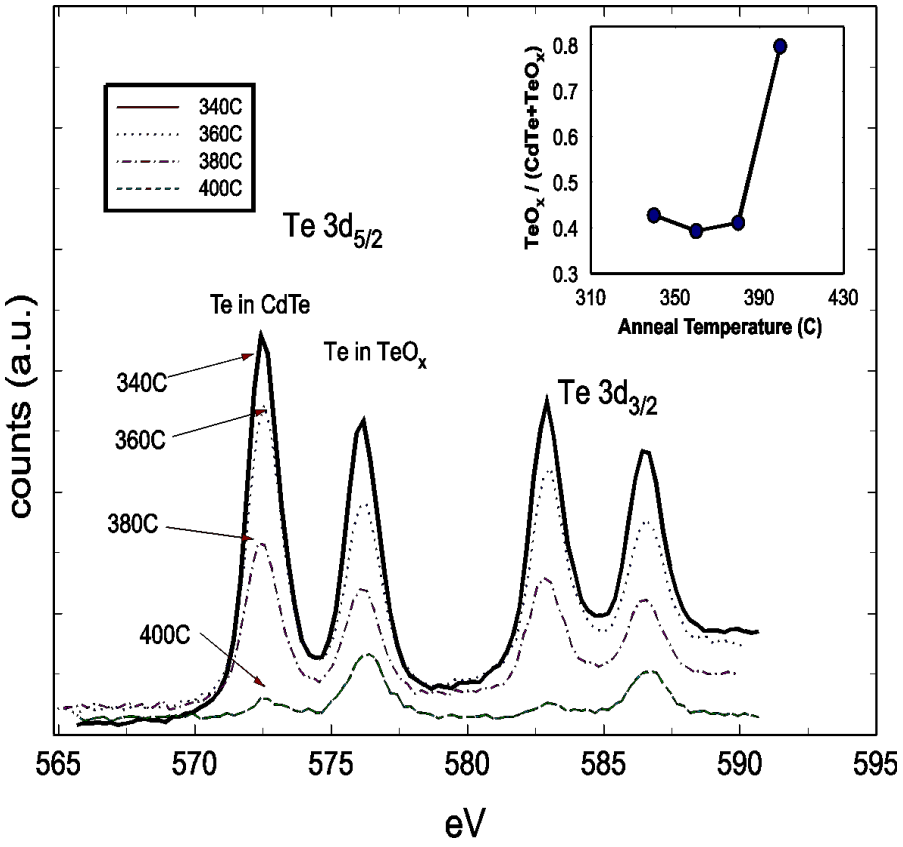

Figure 2.4.1. Te photoelectron peaks from XPS spectra of CdTe annealed at various temperatures. Inset: ratio of TeO_x ($3d_{5/2}$) peak to the sum of the two Te ($3d_{5/2}$) peaks as a function of anneal temperature

2.5 Consumption of CdS during post-deposition processing

Interdiffusion between the CdS and CdTe layers is known to occur during $CdCl_2$ treatment, although the extent of the interdiffusion may depend on the deposition methods for the CdS and CdTe and any post-deposition treatment of the CdS prior to deposition of the CdTe. In the following discussion, we quantify the amount of CdS lost to interdiffusion for the all-sputtered cells grown in our group.

Undergraduate Jennifer Drayton measured the quantum efficiency (QE) and used transmission data from graduate student Diana Shvydka to infer the CdS layer thickness in the CdS/CdTe solar cells after the post-deposition $CdCl_2$ annealing. This was compared with the as-deposited CdS thickness determined from absorption measurements during growth. The results are shown in Figure 2.5.1. The absorption coefficient in CdS is 10.8 μm^{-1} at 450 nm. The data in Fig. 2.5.1 assume that all photons absorbed in the CdS layer do not generate collected carriers. The thickness of the CdTe layer was held constant. The data show a loss of 30-70 nm during $CdCl_2$ processing with some indication that if a thicker layer of CdS is deposited then the amount of CdS that diffuses into the CdTe increases.

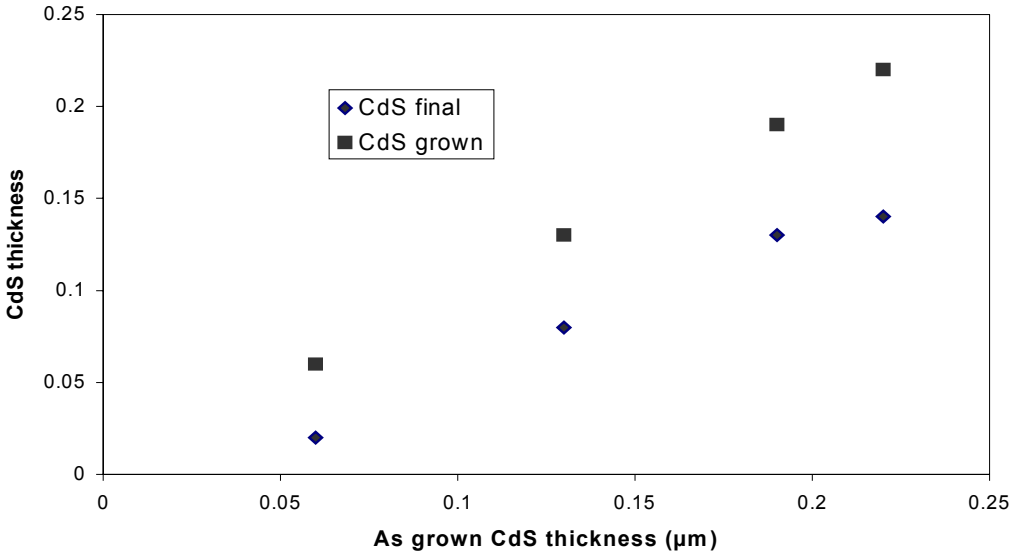

Figure 2.5.1: Final CdS thickness inferred from QE vs. initial CdS thickness

2.6 Cell performance vs. CdTe thickness

High performance CdTe solar cells are typically grown with CdTe thicknesses from 3 to 15 μm, although, from the absorption coefficient one would predict that the thickness necessary for full light absorption should not exceed 0.5 μm, except very near the absorption edge of CdTe. In the following study, we produced a series of cells with different CdTe thickness and held the CdS thickness and contacting procedures constant. Much of this work was performed by summer high school student intern, Jon Smith. A second series of data were obtained by Jennifer Drayton as part of her senior thesis. The second set of data is plotted in Fig. 2.6.1.

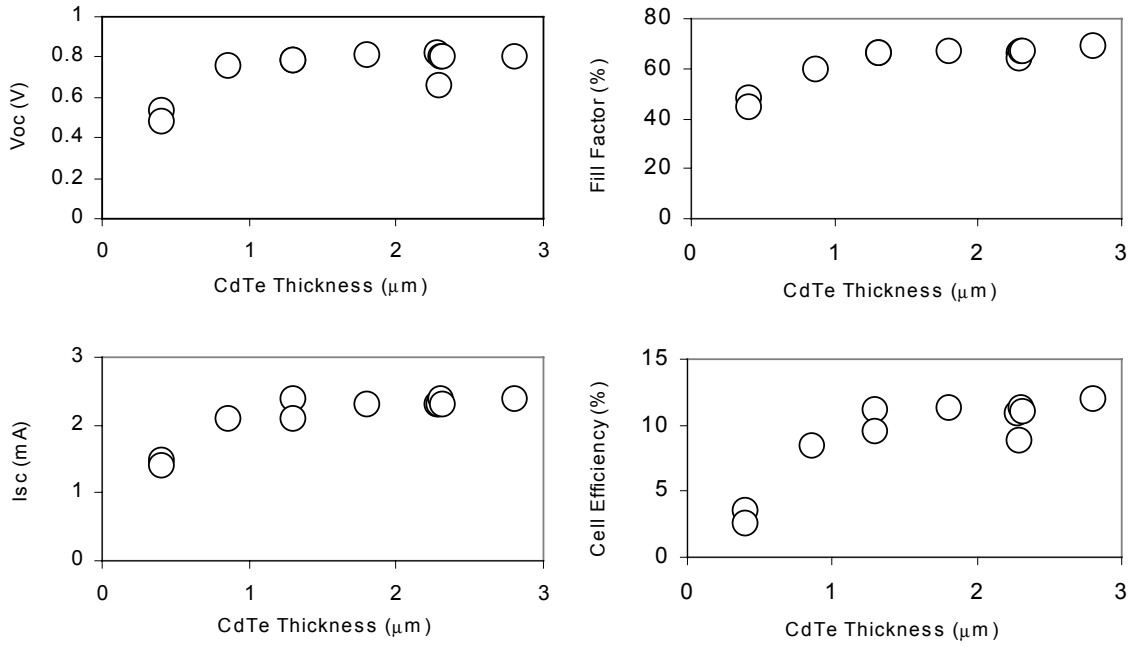

Figure 2.6.1 Cell parameters Voc, Isc, FF, and efficiency vs. CdTe layer thickness

All cell parameters show only slight reductions as the CdTe thickness decreases to 1.3 μm. At 0.8 μm, there is about a 10% reduction in most parameters and somewhat more in the overall cell efficiency. However, below 0.8 μm (at 0.4 μm CdTe thickness) the efficiency drops rapidly as the CdTe is reduced further. Jennifer is presently obtaining quantum efficiency results on these cells to determine the extent of deep penetration loss in the thinner CdTe layers. In addition, we will be monitoring the stability of these cells with reduced CdTe thickness to determine whether the proximity of the back contact, which contains evaporated Cu, will lead to increased degradation .

2.7 Absorption measurements on CdSTe alloy films at 10K

Because of the presence of some CdS_xTe_{1-x} alloy, probably in all CdS/CdTe solar cells, it is important to have a thorough understanding of this material. Therefore we have continued our study of alloy films produced by pulsed laser deposition and have extended it with studies of films deposited by rf sputtering from alloy targets. In the case of the PLD films, we have fabricated our own targets by cold pressing, but for sputtering, we depend on the commercial hot pressed/sintered targets and for this study limited ourselves to the use of just two mixed composition targets. We used targets with an average composition of 4% S and 95% S by atomic percent of anions (i.e., S/S+Te). In other work, we have collaborated with Prof. Pollak's group at Brooklyn College in ellipsometric studies of the optical constants of these alloys. This effort is reviewed in Section 2.9.1 below.

The optical absorption of the CdS_xTe_{1-x} alloy films was measured at both room temperature and at helium temperature (10K). Diana Shvydka measured the specular transmission and reflection spectra of the full range of samples and recently extended her study to films which had been treated in our vapor $CdCl_2$ system. The composition of the films has not yet been tested but based

on our experience with laser-deposited films, we expect the x-values to be very close to those of the average of target compositions.

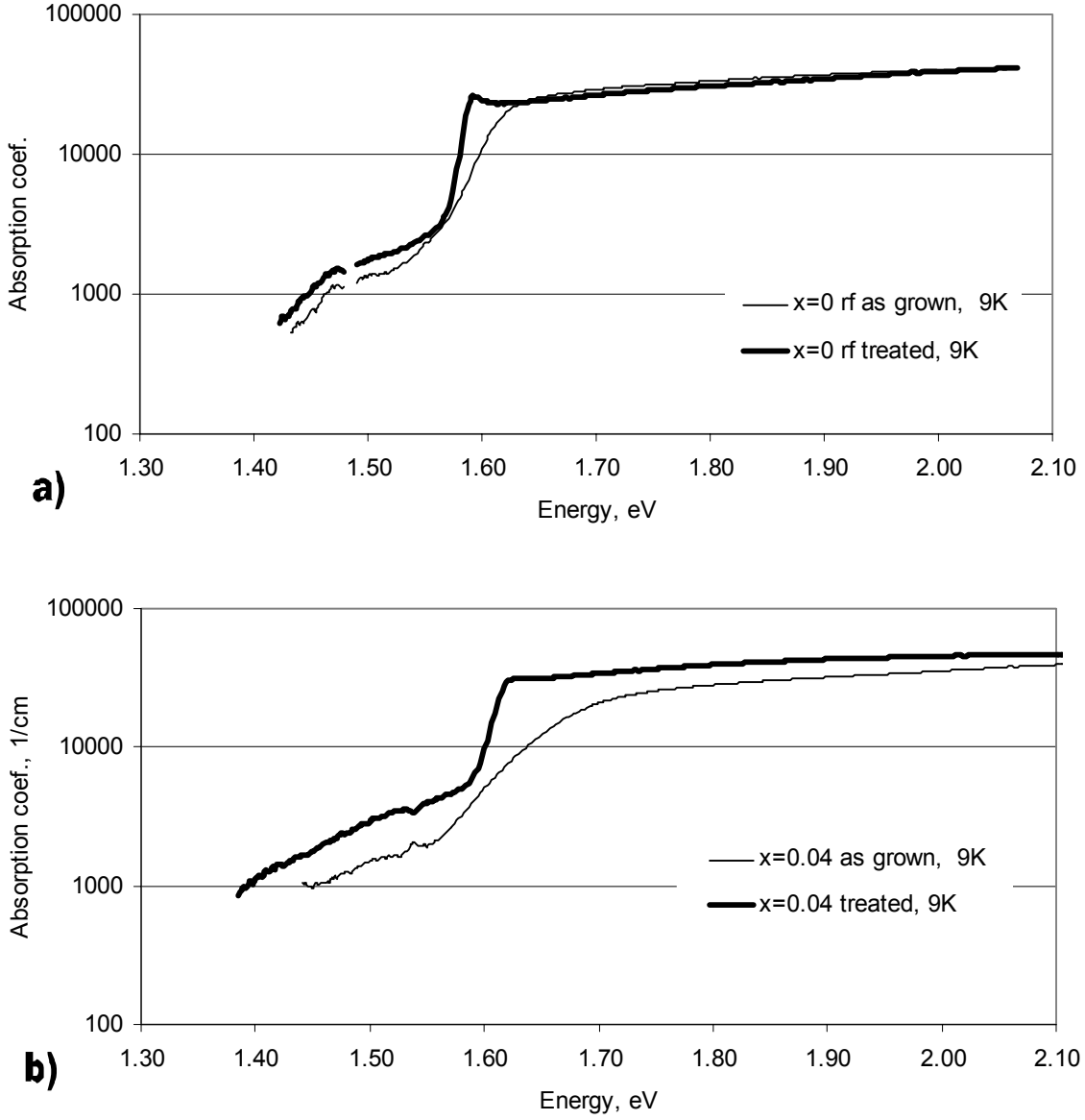

Figure 2.7.1. Absorption coefficient for ~2 μm thick films rf sputtered on Corning 7059 glass before and after vapor $CdCl_2$ treatment. a) pure CdTe; b) CdS_xTe_{1-x} with $x \approx 0.04$

One object of our study is to examine the detailed wavelength dependence of the fundamental absorption edge including the broadenings due to phonons, alloy fluctuations, strains, and inhomogeneities in the films. Because the alloy films are metastable over most of the concentration range and will phase separate upon annealing, Diana has confined her study to the stable regions at the Te-rich end and at the S-rich end. Some results are presented here for films approximately 2 μm thick sputtered at 260° C and for pulsed-laser-deposited films.

Figure 2.7.1a shows the absorption coefficient for pure CdTe sputtered films as-deposited, and after vapor $CdCl_2$ treatment for 30 minutes at 387° C. Figure 2.7.1b provides similar data for alloy films sputtered from targets with x = 0.04, again, before and after $CdCl_2$

treatment. Note that in both compositions, the film quality improves substantially with $CdCl_2$ treatment, so that the exciton peak can clearly be observed. We believe that this is the first time the exciton peak has been seen in a CdSTe alloy film.

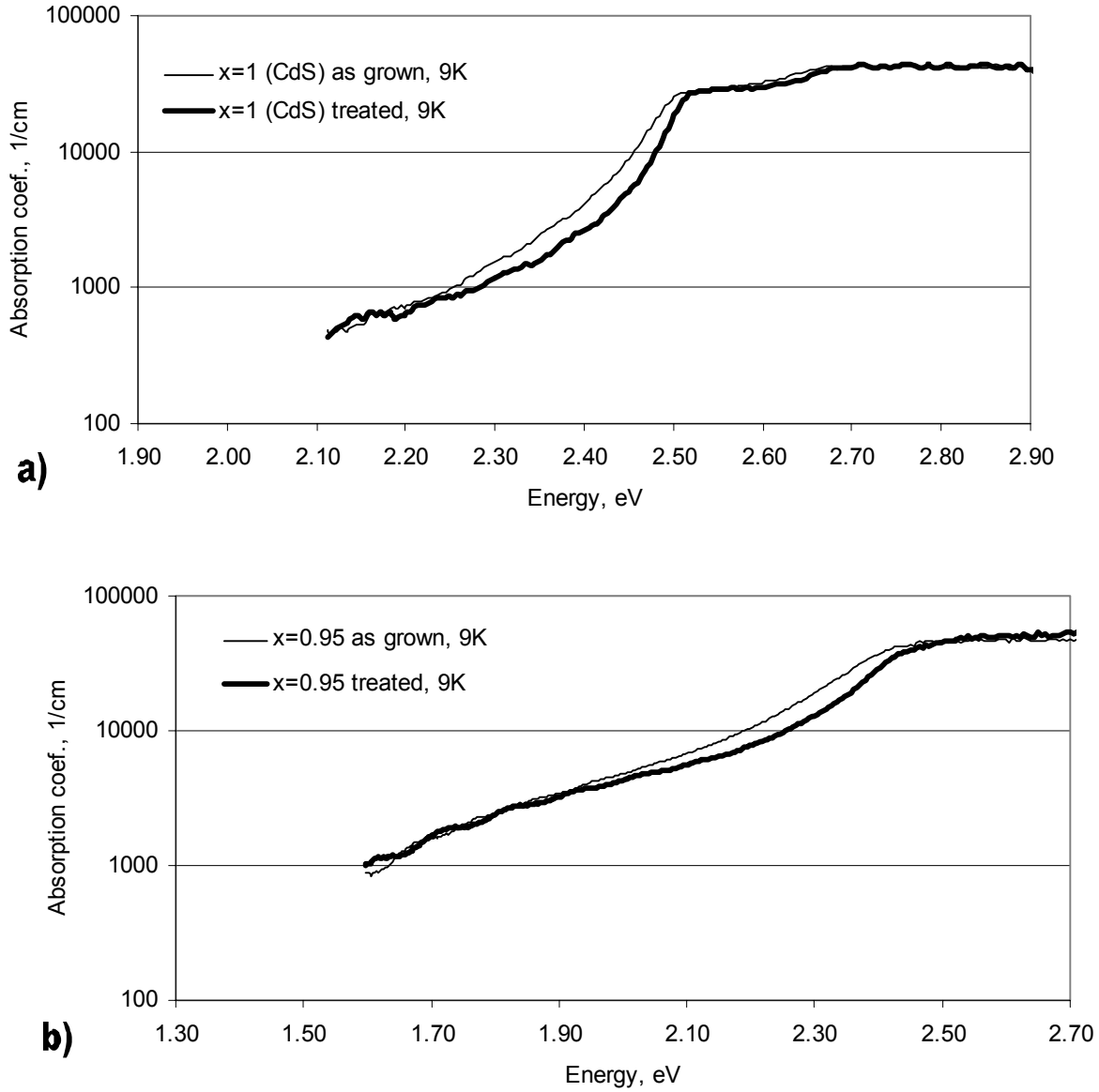

Figure 2.7.2. Absorption coefficient for ~2 μm thick films rf sputtered on Corning 7059 glass before and after vapor $CdCl_2$ treatment. a) pure CdS; b) CdS_xTe_{1-x} with $x \approx 0.95$

For the sulfur-rich sputtered films, Figure 2.7.2 shows again the absorption coefficients before and after $CdCl_2$ treatment. Note that for the pure CdS film there is only slight sharpening of the absorption edge although there is a small blue shift of about 15 meV. In both the as-deposited film and the annealed film, two absorption edges are seen corresponding to the spin-orbit split valence band. Evidence of similar valence band splitting is not seen in the data obtained from the x=0.95 alloy. There appears to be a blue shift of about 30 meV in the absorption curves after $CdCl_2$ anneal treatment, but the tail state density still extends at least 1 eV below the absorption edge of pure CdS.

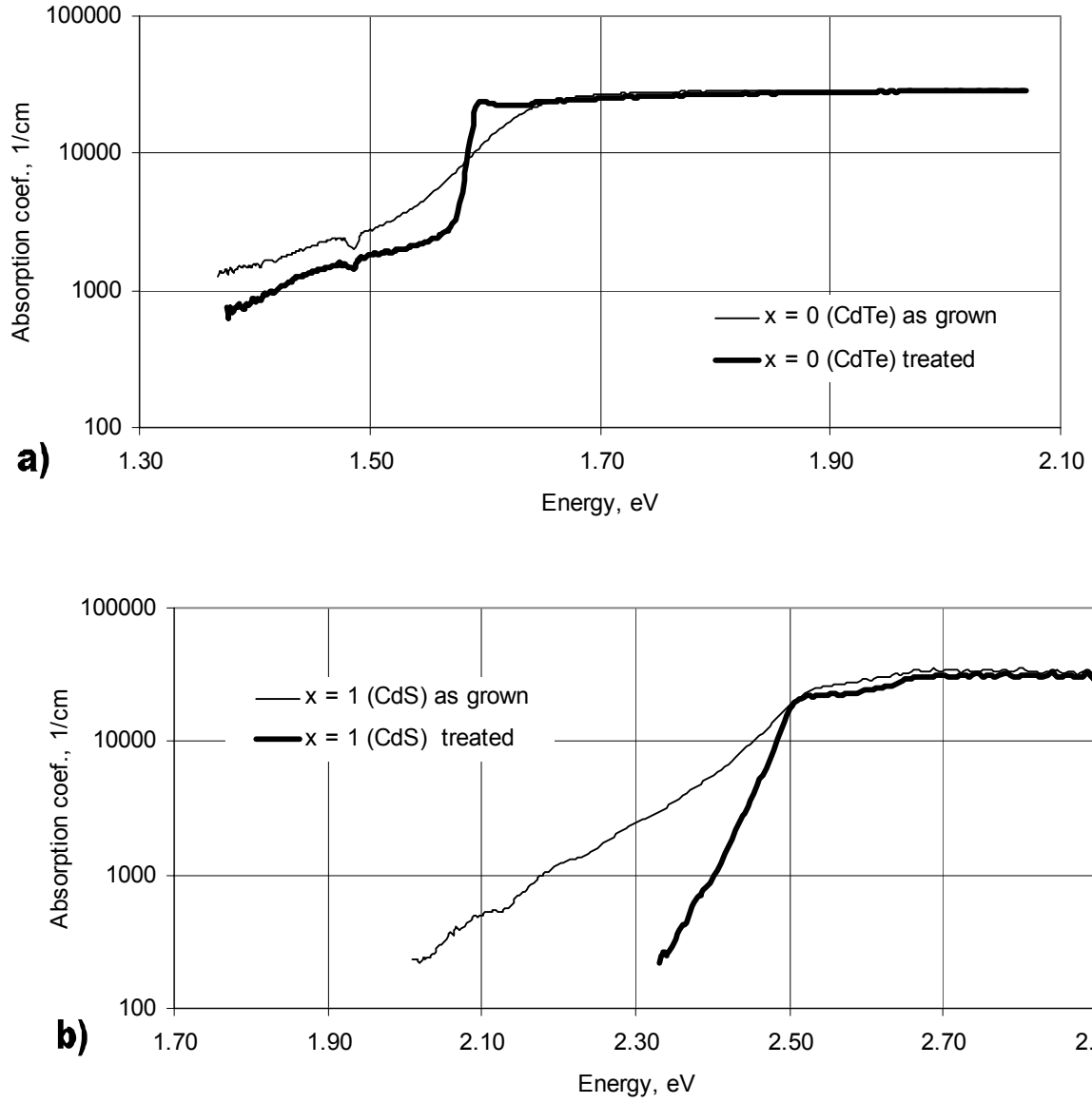

Figure 2.7.3. Absorption coefficient for ~2 μm thick films pulsed laser deposited on Corning 7059 glass before and after vapor $CdCl_2$ treatment. a) pure CdTe; b) CdS

There seems to be a considerable difference in how the absorption edge changes with alloying for S-rich alloys as compared with Te-rich alloys. This may point to the importance of Te-related defect states at low densities in CdS (discussed recently by Zhang, Wei and Zunger) [2.10] and may be related to the lack of observed photoresponse from electron-hole pairs created in the CdS layer of CdS/CdTe solar cells. We expect to examine further this absorption edge behavior in even more lightly CdTe alloyed CdS films.

The same trend of substantial improvement in quality of film with $CdCl_2$ treatment can be observed for pulsed laser deposited films as well. Figures 2.7.3a and 2.7.3b show the absorption coefficient for pure CdTe and pure CdS films as-deposited, and after vapor $CdCl_2$ treatment under the same conditions as before. Again the excitonic feature in CdTe and the valence band

splitting feature in CdS films can be seen after treatment. The tail state density as indicated by the below-band-gap absorption in the as-deposited CdS film is much larger than for the as-deposited sputtered film. This indicates that the film quality of the sputtered films is somewhat higher than for the PLD films.

2.8 Teaming activity

2.8.1 ZnTe-based contacts to CdTe

In this period we participated in stability tests using First Solar CdS/CdTe partial cell structures (complete cell structure except for back contact). Cells using ZnTe/ZnTe:N/Ni, ZnTe/ZnTe:N/Au schemes were sent to First Solar for stress experiments. (Details of the sputtered ZnTe contact structures are provided in Section 2.2.3 above.) As of this writing, the stress test results on our contacts are not available.

2.8.2 Measurements on HRT interfacial layers from Golden Photon

In attempts to improve the efficiency of CdTe-based cells in the blue spectral region, several groups have shown the advantage of thinning the CdS layer, either by depositing a thinner layer or by causing the CdS layer to be nearly entirely consumed by interdiffusion during the $CdCl_2$ treatment process. (See Section 2.5 above.) However, it is found almost always that thinner CdS (below 50 to 80 nm) leads to poorer open circuit voltage and usually poorer fill factors, so that the expected increase in performance is not realized, even though the current is increased with thinner CdS. However, there have been some indications that the use of a resistive coating between the highly doped SnO_2 or ITO and the CdS layer can improve the average V_{OC} and fill factor for cells with thin CdS layers (<50-80 nm). This observation has led to considerable interest in determining the properties of this "high resistivity tin oxide" (HRT). The measurements described in this section were part of a collaborative activity with Peter Meyers from ITN Energy Systems. Peter supplied us with a small piece of the HRT (on borosilicate glass) developed by Golden Photon. Then, near the end of this contract year, we received from him, three types of samples which had an HRT layer deposited at ITN on borosilicate glass. Measurements and comparisons are provided below.

Hall measurements were made on the tin oxide substrate from Golden Photon with a thickness of 0.78 micrometers (measured by profilometry and by optical interference in transmission). Hall measurements were made in the dark and under AM1.5 conditions at room temperature and from 295K to 360K. The material has a room temperature resistivity of 84 Ω-cm in the dark. This was confirmed on at least two occasions by leaving it in the dark for several days since there is evidence of residual conductivity (persistent photoconductivity) after light exposure. The corresponding room temperature light resistivity is about 43 Ω-cm, although there was no attempt to wait for this to reach equilibrium under light conditions. (There was a slow drift toward lower resistivity values with time.) We estimate that the carrier density in the dark is around $3x10^{17}$ /cm^3 and that the mobility is low, of the order of 0.2 cm^2/V-s. We are unable to get reliable Hall measurements with our present system on low mobility materials, but both Hall and thermoprobe measurements indicate the primary carriers to be electrons. Under light conditions it appears that both the carrier density and the mobility increase, but with only a factor

of 3 decrease in the resistivity and with the error limits in the Hall data, this is not a certainty. Finally, the activation energy from 290K to 360K for the dark conductivity is about 0.085 eV in both light (AM1.5) and dark.

We can conclude that this material is similar in behavior to some of the laser-grown CdS films showing a low mobility and the presence of long recombination times.

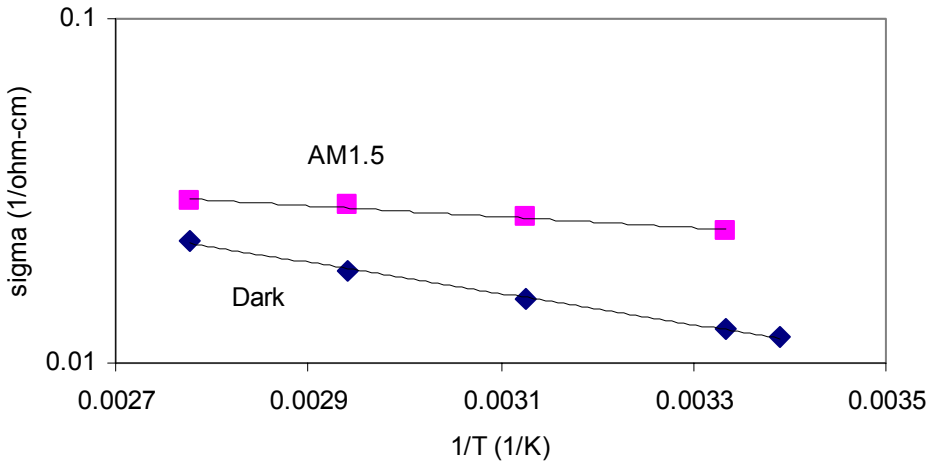

Figure 2.8.1 Conductivity vs. 1/T for GPI HRT material. The straight line fits yield activation energies of 0.087 and 0.084 eV for the conductivity in the dark and light, respectively.

2.8.3 Hall Measurements on ITN HRT Samples

Hall effect measurements were done on the three samples from ITN which were classified as intrinsic (90226c), doped nominally with 1% Cd (90222b), and doped with 1% Zn (90209b). (SIMS measurements showed 0.6% Zn incorporation.) Room temperature measurements were made on all the samples as well as measurements from about 280K to 355K. The data obtained at 300K are summarized in the table below. Results on the GPI sample and an LOF sample are included for comparison.

Table 2.8.1 Hall measurements on HRT substrates

Sample	Thickness (μm)	Resistivity (Ohm-cm)	Carrier Density (cm^{-3})	Mobility (cm^2/V-s)	E_{act} (eV)
ITN Intrinsic	0.89	0.053	2.2E19	5.6	0.010
ITN 1% Cd	0.70	0.98	2.9E18	2.2	0.042
ITN 1% Zn	0.62	43.	5.5E17	0.26	0.096
GPI	0.78	84	3.7E17 (est)	0.2 (est)	0.087
LOF (8 Ω/sq)	0.68	5E-4	4.0E20	31	-

Estimated uncertainties for the resistivities are less than 5%. Estimated uncertainties for the carrier densities range from less than 8% for the intrinsic and the LOF sample, to as high as 100% for those samples with mobilities less than one. We have thus far been unable to get reliable measurements on low mobility materials.

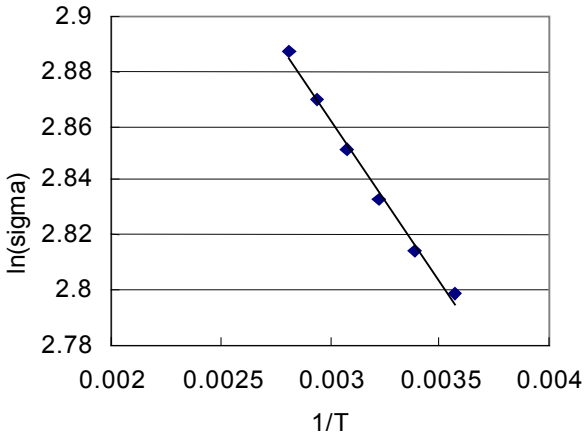

Figure 2.8.2. Semi-log plot of the conductivity in units of $(ohm\text{-}cm)^{-1}$ vs. 1/T of the intrinsic HRT sample from ITN. Straight line shows the fit to an activation energy of 0.010 eV.

It would appear that the addition of Cd to the intrinsic material reduces the carrier density by an order of magnitude and the mobility by about a factor of two. The addition of Zn has a more dramatic effect reducing the carrier density by about a factor of 40 and the mobility by a factor of 20. It should be noted that the primary difference between the 1% Zn sample properties and the Golden Photon sample seems to be the carrier density.

Table 2.8.1 also shows the activation energy for the conductivity as determined from the measurements between 280K and 355K. Because of the uncertainties it was not possible to determine the activation energies for the carrier density or the mobility. For the intrinsic material the conductivity changed by less than 10% over the temperature range.

A conductivity versus 1/T plot for the intrinsic sample is shown as an example. The activation energy for the LOF material is not given since it appears to be a degenerate semiconductor over an extended temperature range. It should be noted that the activation energy for the Golden Photon material and the 1% Zn sample are similar, which is consistent with the similarities in the other measured properties.

2.8.4 Cell Performance with Reduced CdS Thickness on Glass/TCO/HRT

In addition to the Hall measurements of HRT films on BSG substrates, we have participated in the teaming activity on the investigation of the effect of a high-resistivity tin oxide (HRT) layer that is deposited on the regular, more conductive, fluorine-doped tin oxide. The substrates were made by Peter Meyers at ITN Energy Systems Inc. (Wheat Ridge, Colorado) and consisted of Zn/Cd doped or undoped HRT deposited by spray pyrolysis on LOF TCO coated glass. The HRT thickness was approximately 0.8μm.

It is desirable to thin the CdS window layer to improve the short wavelength spectral response, which raises the current. The HRT film helps to prevent the CdTe-TCO contact in the case of pinholes in thin CdS. Another benefit may lie in the fact that the resistivities of CdS and HRT roughly match.

Figure 2.8.3 shows typical J-V curves for different thicknesses of CdS. Increased CdS thickness improves the open circuit voltage considerably, but the short circuit current decreased a little bit as the as-deposited CdS thickness went up from 60 to 120 nm. Note that the blocking diode or rollover behavior can result from changes at the junction region!

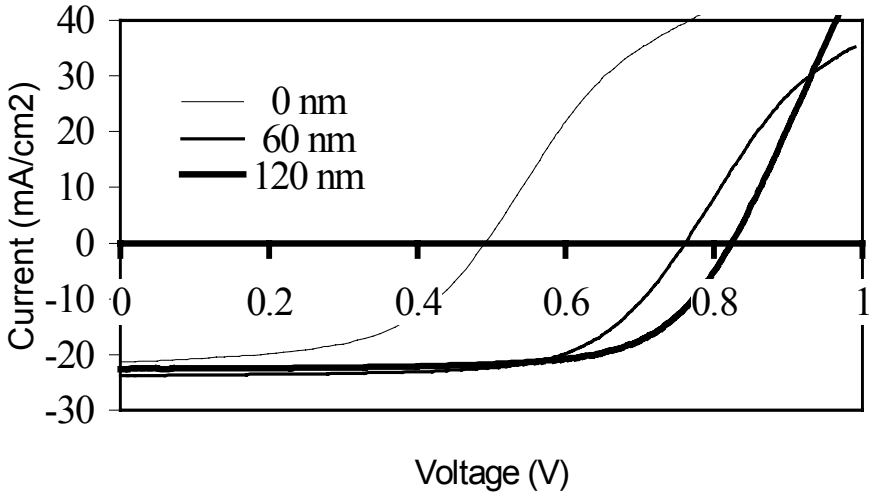

Figure 2.8.3. The J-V curves of solar cells made on substrates with undoped HRT film. As-deposited CdS of 60 and 120 nm reduced to 30 and 80 nm after $CdCl_2$ processing.

Figure 2.8.4 displays the spectral quantum efficiencies (SQE) for cells made on Zn and Cd doped HRT. Clearly, the blue response increases as the CdS gets thinner, although the zero CdS cells have reduced overall performance due to the missing n-CdS/p-CdTe junction. The SQE curves allow us to determine the amount of CdS that did not diffuse into the bulk of CdTe. (See Section 2.5.) The original 60 nm thickness decreased to 30 nm and 120 nm went down to about 80 nm.

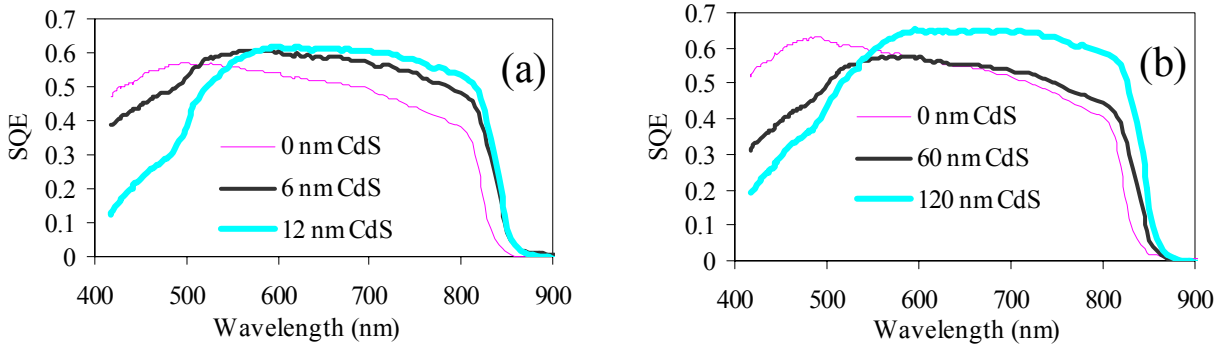

Fig. 2.8.4. Spectral quantum efficiencies of cells made on (a) Zn and (b) Cd doped HRT.

Non-stress 18 day stability test results are shown in Figure 2.8.5. Zero CdS thickness cells deteriorated the most. Cells with as-deposited 60 and 120 nm of CdS on undoped HRT (Fig. 2.8.5(a)) were quite stable. See Table 2.8.2 for the complete performance data.

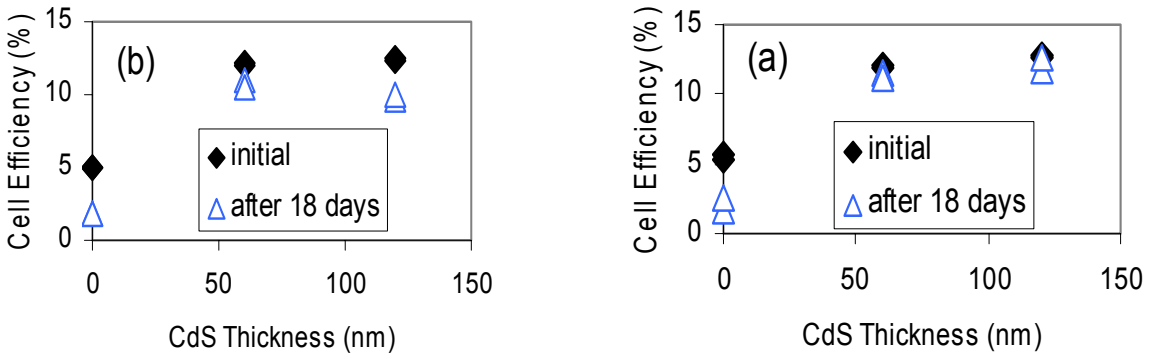

Fig. 2.8.5. Cell efficiency degradation after 18 days on shelf for (a) undoped and (b) Cd-doped substrates.

Table 2.8.2 presents the Voc, Isc, fill factor, and cell efficiency data for the best contact (representative of overall performance) from each type of substrate and three different CdS thicknesses.

Table 2.8.2. Summary of Cell Performance for Four Substrate Types and no CdS, 60 nm, and 120 nm of as-deposited CdS for Each HRT Type.

HR film	CdS thickness	Voc		Isc		Fill Factor		Efficiency	
		V		mA/cm2		%		%	
	nm	initial	+18 days	initial	+18 days	initial	+18 days	initial	+18 days
none	0	0.38	0.19	20.1	17.4	54	37	4.1	1.2
	60	0.63	0.56	24.1	24.5	66	63	9.9	8.7
	120	0.81	0.81	22.5	23.0	67	66	12.3	12.3
Undoped	0	0.49	0.25	21.4	19.2	54	34	5.7	1.6
	60	0.76	0.74	23.8	23.8	66	65	12.0	11.5
	120	0.82	0.81	22.6	23.4	69	62	12.8	11.8
Zn doped	0	0.69	0.62	20.2	15.8	36	26	5.1	2.6
	60	0.84	0.81	23.2	22.7	56	49	11.0	9.1
	120	*0.83	0.82	*23.0	24.5	*46	53	*8.8	10.7
Cd doped	0	0.46	0.29	21.6	18.1	50	35	5.0	1.8
	60	0.83	0.80	22.0	22.3	67	62	12.2	11.0
	120	0.82	0.80	22.8	23.9	66	51	12.4	9.7

*probably a measurement error

2.9 Collaborative Activity

There have been three substantial collaborations with groups outside the National CdTe Photovoltaic Team during the period of this report. These collaborations include 1)

spectroscopic ellipsometry studies of the CdS_xTe_{1-x} alloy system with Prof. Pollak from Brooklyn College, 2) grazing incidence x-ray fluorescence studies of CdS/CdTe bilayers at the Brookhaven National Synchrotron Light Source (NSLS) with Prof. Kao from the Univ. of Buffalo, and 3) laser scribing studies on non-vacuum deposited CIGS with International Solar Electric Technologies (ISET).

2.9.1 Ellipsometry of CdSTe alloy films (collaboration with Brooklyn College)

This work was a collaboration between UT and Brooklyn College in which we supplied a collection of CdS_xTe_{1-x} alloy films deposited on borosilicate glass at 260 ^oC by XeCl excimer pulsed laser deposition. The room temperature optical absorption of many of these films were obtained earlier by Ramesh Dhere and David Abin. (We presented their data in our Final Technical Report for Subcontract ZAX-4-14013-4.) [2.1] The collaboration with K. Wei and Fred Pollak at Brooklyn College made possible the acquisition of a full range of data on the complex dielectric constant of these alloys over the range from 0.75 to 5.4 eV. J.L Freeouf of Interface Studies, Inc., was also a collaborator. A manuscript describing this work in more detail has appeared in the Journal of Applied Physics.[2.8]

The bulk complex dielectric function $\varepsilon(E) = \varepsilon_1(E) + i\varepsilon_2(E)$ data, obtained by spectral ellipsometry, reveal distinct structures associated with critical points (CPs) related to E_0 (direct gap), the spin-orbit split $E_0 + \Delta_0$, the E_1 and $E_1 + \Delta_1$ doublet, and the E_2. The experimental data over the entire measured spectral range (after oxide removal) was fit using a model dielectric function based on the electronic energy-band structure near these CPs *plus excitonic and band-to-band Coulomb enhanced (BBCE) effects*. In addition to evaluating the energies of these various band-to-band CPs, our analysis also makes it possible to obtain information about the binding energies (R_0, R_1 respectively) of not only the three-dimensional (3D) exciton associated with E_0 but also the two-dimensional (2D) exciton related to the E_1 and $E_1 + \Delta_1$ CPs.

The two-dimensional critical point and associated two dimensional exciton typically arises in zincblende crystals due to a region in crystal momentum space (k-space) where the valence and conduction bands are parallel along the [100] or [111] (X or Δ) directions in k-space. This leads to an infinite effective mass component in the joint density of states. As a result, the exciton binding energy is significantly enhanced, similar to the behavior in quantum-well structures where quantum confinement occurs in one dimension.

The results of this experiment demonstrate conclusively that the correct band-to-band lineshape at E_0 is BBCE, even if the exciton is not resolved, and not the single particle lineshapes used previously. Thus the band-edge energies are slightly modified when the coulomb effects including the exciton are included.

The ellipsometric measurements were made at room temperature using an Instruments SA spectroscopic phase modulated ellipsometer. The samples were measured in as-received condition, then the S (Te) rich samples were etched in a 10% solution of HF in H_2O (50% HCl solution in methanol), until the spectra showed no change after further etching (about 1 minute). The samples were measured at three angles of incidence, 65^o, 70^o, and 75^o. The data and fits for several of the samples are shown in Figures 2.9.1 and 2.9.2 for the imaginary and real parts of the dielectric constant respectively.

Highlights of the ellipsometric results include the following:

1. the exciton binding energy at the fundamental gap (R_0) increases from 10 meV for CdTe to 27 meV for CdS in agreement with other measurements;

2. the E_1 exciton (two-dimensional) binding energy (R_1) increases from 145 ± 40 meV for CdTe to 205 ± 30 meV for CdS;
3. the band bowing of the E_1 critical point is much smaller than that of the E_0 fundamental edge; (See discussion and figures below.)
4. the E_1 critical point energy rises more rapidly than the E_0 energy as the sulfur content increases; and
5. the real part of the dielectric constant below the fundamental gap (0.75 – 1.4 eV) can be approximated by the Sellmeir equation,

$$\varepsilon_1(E) = n_0^2 + [bE_a^2/(E_a^2 - E_0^2)],$$

with, for CdTe, $n_0^2 = 6.37$, $b = 0.91$, and $E_a = 1.80$ eV.

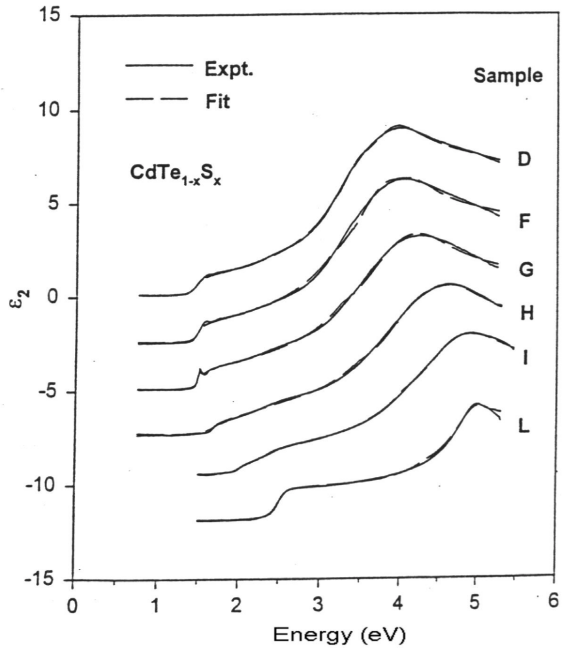

Fig. 2.9.1. Solid lines are $\varepsilon_2(E)$ for samples D (x=0.20), F (x=0.29), G (x=0.48), H (x=0.70), I (x=0.90), and L (x=1). Dashed lines are fits using the band-to-band coulomb enhanced (BBCE) model. The curves for the latter five samples are each displaced by -2 units for clarity

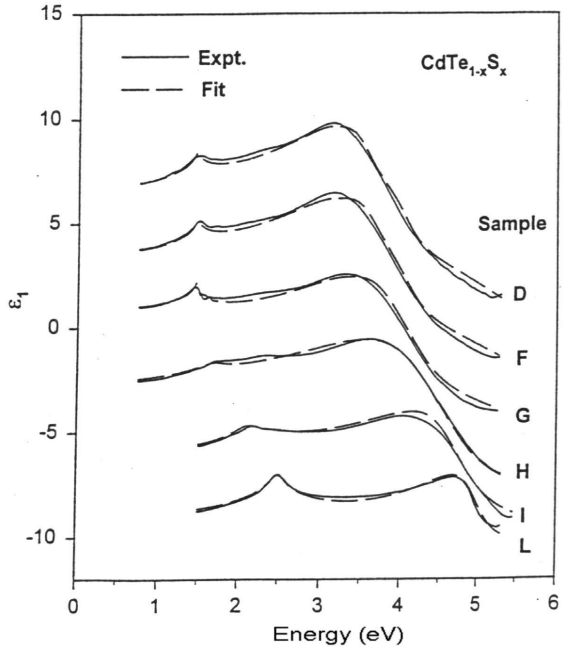

Fig. 2.9.2. Solid lines are ε_1 for samples D, F, G, H, I, and L. Dashed lines are fits using the band-to-band coulomb enhanced (BBCE) model. The curves for the latter five samples are each displaced by -2 units for clarity.

The values of the E_o and E_1 band edges obtained by fitting the ellipsometric data with the BBCE lineshapes are shown in Figures 2.9.3 and 2.9.4. We also show the best fits obtained for the x-dependence, assuming a simple bowing parameter defined below. The band gap energy or critical point energy as a function of the sulfur (x-value) is defined by

$$E(x) = E(CdTe) + x[E(CdS) - E(CdTe)] - Cx(1-x) = E(CdTe) + Bx - Cx(1-x),$$

where C is the bowing parameter. Note that, for the E_o fundamental gap, the data cannot be fit very well with a single bowing parameter, C. For the E_0 edge the bowing parameter was found to be C = 1.84, slightly higher than the C=1.7±0.1 as obtained from absorption measurements where we did not include the coulomb effects. For the E_1 edge the data indicate C=0.8. From pure CdTe to pure CdS, the E_0 position increases from 1.54 eV to 2.48 eV (B = 0.94 eV) whereas the E_1 critical point rises from 3.34 eV to 4.92 eV (B = 1.58 eV).

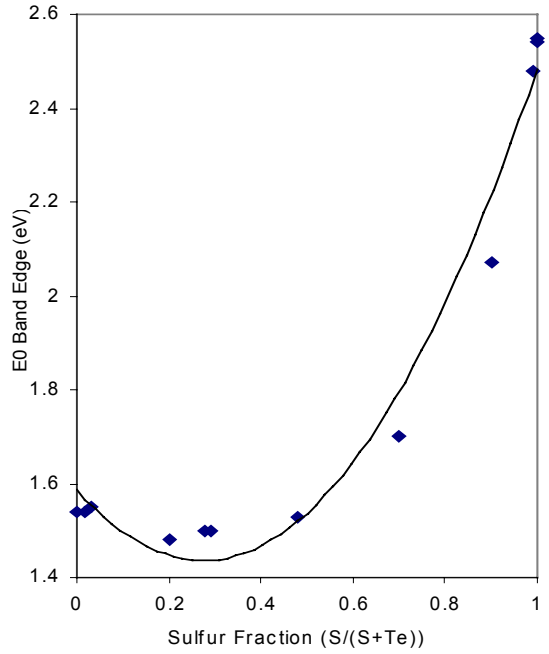

Fig. 2.9.3. Dependence of fundamental band gap energy E_0 on sulfur fraction. Solid line is a quadratic fit. (See text.)

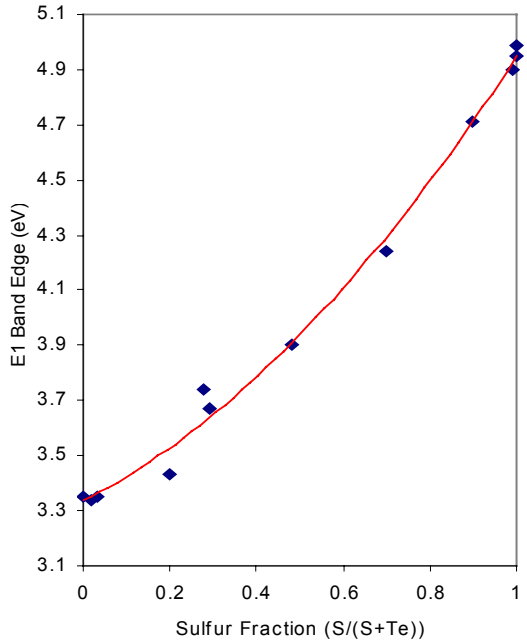

Fig. 2.9.4. Dependence of E_1 band edge energy on sulfur fraction. Solid line is the quadratic fit. (See text.)

Additional details of the ellipsometry measurements and the analysis are included in the published manuscript.[2.11]

2.9.2 Grazing incidence x-ray fluorescence of annealed CdS/CdTe bilayers

The grazing incidence x-ray fluorescence techniques were described in some detail in our Final Technical Subcontract Report for 1997. This collaborative work with the group of Yi-Han Kao has now been published in the Applied Physics Letters, **74**, 218 (1999). The article is titled: "Annealing Effects and Te Mixing in CdTe/CdS Heterojunctions," by Y.L. Soo, S. Huang, Y.H. Kao, and A.D. Compaan. [2.12] The x-ray fluorescence measurements used the Bookhaven synchrotron with photon energy of 31.9 keV on sputtered bilayer films having the structure BSG/CdTe/CdS with semiconductor layers of about 20 nm thickness. This choice of photon energy is just above the Te K-shell ionization energy of where the index of refraction is slightly less than unity. Grazing incidence angles ranged from 0.01 to 0.20 degrees providing controllable penetration depths of the evanescent x-ray wave ranging from 3 nm up. Changes in the Te K_α fluorescence at 27.472 keV relative to the Cd K_α fluorescence at 23.174 keV indicate that a major amount of diffusion of Te to the surface occurs for temperatures above 370^o C when $CdCl_2$ vapors are present. These temperatures correspond closely to the point at which solar cell performance improves in our sputtered cells.

Collaborations with the group of Y.H. Kao are continuing and have been extended to include extended x-ray absorption fine structure (EXAFS) in studies of the lattice location of Cu in ZnTe and Cu in CdTe. Results will be reported as they become available.

2.9.3 Laser scribing

The principal laser scribing collaborative activity for the past year was the search for optimum parameters for the CIS (copper indium diselenide) layer removal from the underlying layer of molybdenum. Although the melting temperature of Mo is much higher than CIS, we found that for most situations the Mo was easily damaged (usually badly cracked or pieces which flaked away) in the process of exposing a clean Mo surface to enable deposition of a ZnO interconnect layer. We have found the best results with the long-pulse IR YAG laser. Fig. 2.9.5 shows optical micrographs and profilometer traces of such a scribes in CIGS/Mo/glass samples from two different sources. Note the smooth, clean bottom of the scribe which appears to self-limit at the Mo interface. Our interpretation is that the higher melting temperature and the much higher thermal diffusivity of the Mo enable the Mo layer to remain solid for the long pulses (~250 nsec) of this YAG laser

Also, we received a request from the International Solar Electric Technology, Inc. (ISET - Inglewood, CA) to optimize the simultaneous scribing of both CIS and Mo films. Parallel scribes with 5-6 mm spacing are a first step in the “post absorber” type module fabrication [2.13]. The goal was to achieve complete isolation between the resulting pads with the minimal melt area along the scribes. Since the total thickness of both films was over 3 μm, we used the glass-side scribing where the vapor created at glass-film interface blows off the rest of the film.

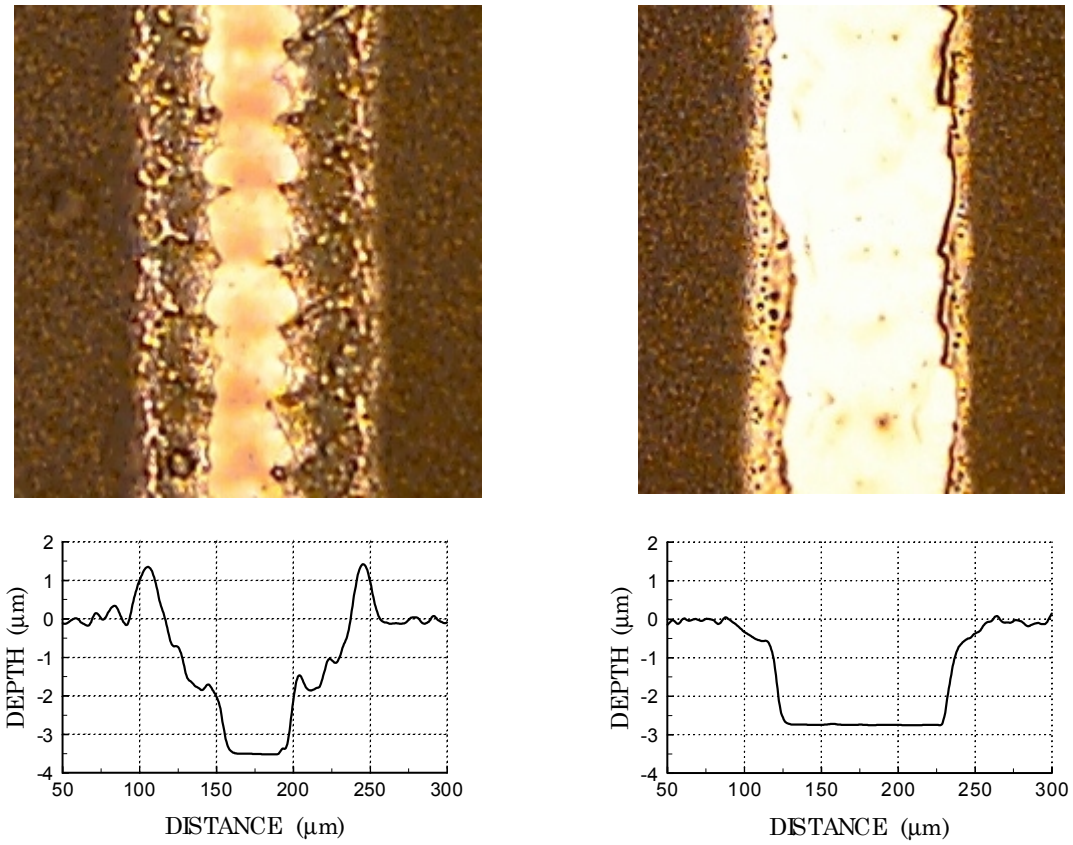

Fig. 2.9.5. Optical micrographs and profiles of YAG laser (1064 nm, 250 ns) scribes of CIS on Mo with 4.2 J/cm^2, 25 mm/s (left) and 2.4 J/cm^2, 1 mm/s (right). CIS thicknesses of 3.6 and 2.7 μm respectively.

The first attempt at scribing of both Mo and CIS layers was made using a Quantronix continuous-lamp-pumped Nd:YAG 1064 nm laser which had 500 Hz repetition rate and pulse duration of 250 ns. A 16 cm focal length spherical lens was used. The resulting electrical isolation was about 3 MΩ, but it deteriorated to several kΩ in one hour. The energy density in the center of a pulse was 5 J/cm^2, translation speed 1.8 mm/s, and spot diameter 60 μm. We believe that the long pulse duration and, secondarily, the higher repetition rate caused larger areas around the scribe and the glass to heat up. This may have resulted in some evaporation of CIS elements, which then formed a very thin conducting film or doped the glass in the scribe area. On the other hand, the spherical lens produces a circular spot, which ejects the material in all directions including the side of completed scribe that may get contaminated this way. Cylindrical focussing doesn't have this problem (see below).

A short pulse (10 nsec) flashlamp-pumped Nd:YAG 1064 nm laser was utilized for the next trial. Acceptable isolation (better than 40 MΩ) which didn't deteriorate with time has been achieved using a 6 cm focal length cylindrical lens (see Fig. 2.9.4). After some test runs using 8 J/cm^2 intensity it was found that the highest translation speed that yields a good scribe was 6 mm/sec at 10 Hz – higher repetition rate would allow for the proportionally higher speed as long as local overheating doesn't degrade the scribe quality.

Although laser scribing is not a principal focus of our efforts in this contract, we continue to maintain some capability to perform scribing tests on a variety of materials at the request of the thin-film photovoltaics research community. We are currently providing some assistance to the NREL CIGS group in setting up a Kr-lamp pumped, frequency–doubled Nd:YAG laser system.

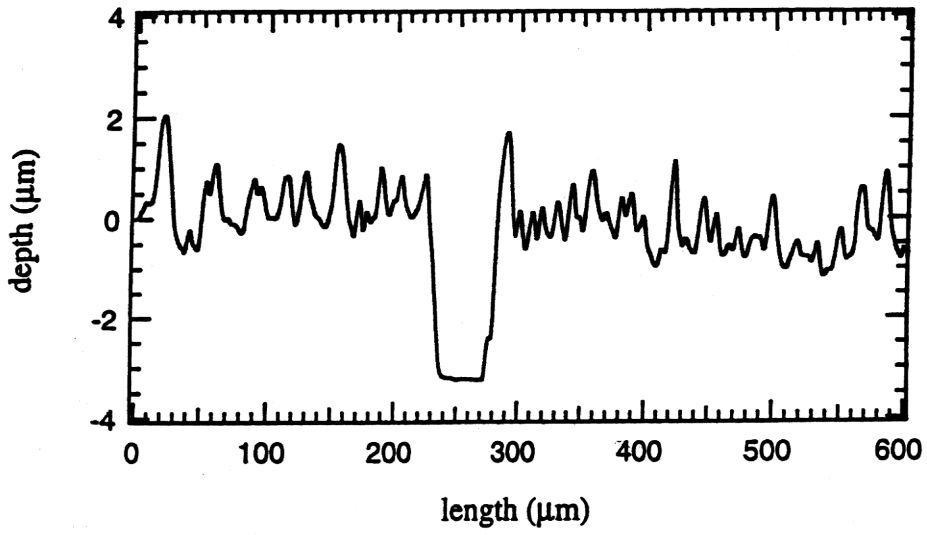

Fig. 2.9.6 A Dektak profilometer trace of Nd:YAG (10 nsec) laser scribe through CIS and Mo (total thickness about 3 μm). Translation speed was approximately 1 mm/sec.

2.10 Conclusions/Future Directions/Acknowledgments

Promising results have been obtained in Phase I with the reactive sputtering of ZnTe:N for a back contact transition layer especially on wet-treated First Solar material. Extension of these results to vapor treated CdTe grown by vapor transport deposition and by RF sputtering will receive strong emphasis. These efforts will include the use of metals other than Ni as the back contact to the ZnTe:N and possibly some interfacial treatments. In addition, we shall focus on achieving some doping of the CdTe, especially at the back contact. The objective is to achieve a high quality, stable, and manufacturable back contact to polycrystalline CdTe.

We shall continue to explore the role of copper in CdTe with the goal of greatly improved understanding of the lattice location, electrical properties, and movement of Cu as a functoin of temperature and E-fields. This effort will utilize primarily photoluminescence but will include Hall measurements, EXAFS, cell performance changes, and other techniques as appropriate. We will continue to maintain focus on improved understanding of factors which affect stability including the role of copper in CdTe and CdS as well as interdiffusion at the CdS/CdTe interface.

Optical studies, including PL and absorption, of the CdSTe alloy system will emphasize the changes in properties of the almost pure binaries, CdTe and CdS, with trace amounts of S or Te, respectively. Our capability for laser scribing with excimer and Nd:YAG laser systems continues to be available to the thin-film PV community. We shall continue full participation in

the National CdTe PV Team and continue our involvement with several other outside collaborators.

We are grateful to Kent Price, postdoc, for much work in preparing this report. Many individuals, in addition to those at the University of Toledo, listed under Project Personnel, have contributed substantially to our success in the past year. This includes Gary Dorer, Upali Jayamaha, R.C. Powell, Doug Rose, and others at First Solar, LLC. All the members of the National CdTe PV team have been important in one or more projects reported here—from exchange of samples to illuminating discussions. We especially thank LOF for a supply of superstrate material and Chris Ferekides (USF) and Pete Meyers (ITN) for other superstrates with HRT layers. We are especially grateful to NREL for support and to Bolko von Roedern, our contract monitor for his support and advice.

2.11 References

2.1 A.D. Compaan, & R.G. Bohn, *High Efficiency Thin-film Cadmium Telluride Photovoltaic Cells*, Annual Subcontract Report for the period 1/21/97-3/31/98, Contract No. ZAX-4-14013 [available from NTIS, publication NREL/SR-520-25856] (41 pages)

2.2 A. D. Compaan, R. G. Bohn, *Thin-film Cadmium Telluride Photovoltaic Cells, Final Subcontract Report, 1 November 1992 to 1 January 1994* (available NTIS publication NREL/TP-451-7162; DE 94011886).

2.3 Xianda Ma, M.S. Thesis: "ZnTe:N Film as a Back-Contact Material for Solar Cells" (May 1999, U. of Toledo, unpublished)

2.4 I. Lyubomirsky, M.K. Rabinal, D. Cahen, *J. Appl. Phys.* **81**, 6684 (1997)

2.5 J.P. Laurenti, G. Bastide, M. Rouzeyre, R. Triboulet, *Solid State Comm. **67**, 1127 (1988)*

2.6 H. Uda, S. Ikegami, H. Sonomura, *Sol. Energy Mater. Sol.Cells* **50,** 141, (1998)

2.7 D. Grecu and A.D. Compaan, "Photoluminescence Study of Cu Diffusion and Electromigration in CdTe," Appl. Phys. Lett. **75**, 361-363 (1999).

2.8 D.M. Waters, D. Niles, T.A. Gessert, D. Albin, D.H. Rose, P. Sheldon, 2nd World Conference and Exhibition on Photovoltaic Solar Energy Conversion, Vienna, Austria, 6-10 July 1998, pp. 1031-1034

2.9 *Practical surface analysis : by Auger and x-ray photo-electron spectroscopy* edited by D. Briggs and M.P. Seah, Chichester ; New York : Wiley, (1983).

2.10 S.B. Zhang, S.-H. Wei, and A. Zunger, Phys. Rev. Lett. **78**, 4059 (1997).

2.11 K. Wei, F.H. Pollak, J.L. Freeouf, D. Shvydka, and A.D. Compaan, "Optical Properties of $CdTe_{1-x}S_x$ ($0 \le x \le 1$): Experiment and Modeling," J. Appl. Phys. **85**, 7418-7425 (1999)

2.12 S. Huang, Y.L. Soo, Y.H. Kao, and A.D. Compaan, "Annealing effects and Te mixing in CdTe/CdS heterojunctions," Appl. Phys. Lett., **74**, 218-220 (1999).

2.13 S.Wiedeman, R.G.Wendt, J.S.Britt, "Module Interconnects on Flexible Substrates," NCPV PV Program Review, 1998, (AIP CP462) p. 17.

3 Amorphous Si-Based Solar Cells and Materials

3.1 Introduction

Significant progress has been made recently in a-Si photovoltaic research and manufacturing using a triple-junction structure [3.1-3.4]. These include the achievement of 15.2% initial efficiency for small area solar cells [3.1], 13% stable efficiency for small area solar cells [3.2], 10.2% stable efficiency for 1 ft^2 solar panels [3.3] and 8% stable efficiency for 4 ft^2 production scale PV modules [3.4]. However, to meet the long term efficiency (>15%) and cost (<\$50/m^2) goals [3.5], further improvement in the materials and device structure for the high efficiency triple-junction solar cells is still needed.

We focus our study on some long term issues related to high efficiency multiple-junction a-Si based solar cells. During the past year, one of our emphases was to establish a good baseline for the fabrication of high efficiency a-Si-based single- and triple-junction solar cells.

The device structure for single and triple cells are shown in Figure 3.1.1 (a) and (b). These devices were deposited on bare stainless steel (SS) substrates or back-reflector (Ag/ZnO) coated SS substrates. These substrates were provided by Energy Conversion Devices, Inc. (ECD).

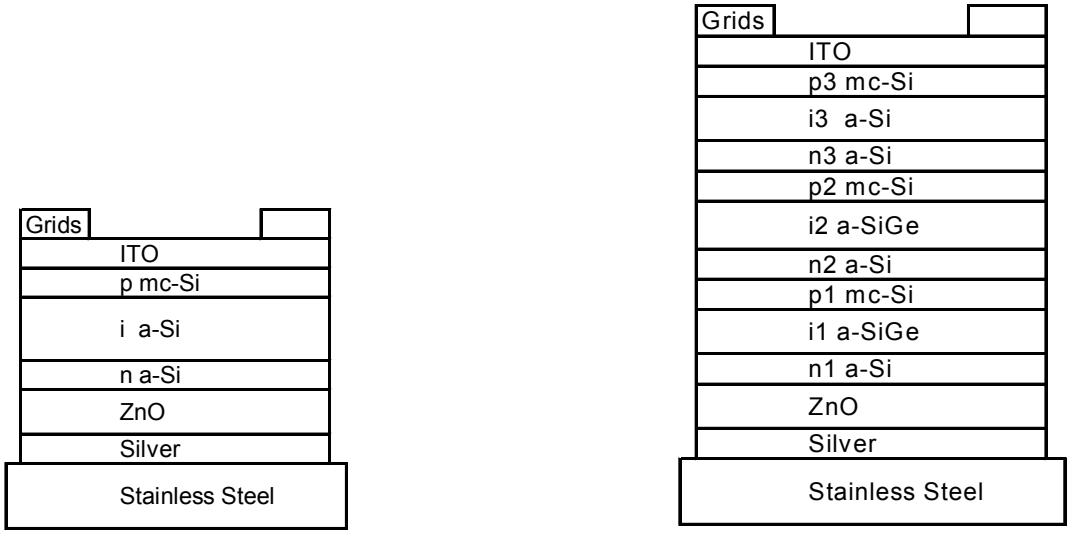

Figure 3.1.1. Schematics of the single-junction (a) and triple-junction (b) structures of a-Si solar cell devices fabricated in this program.

Amorphous silicon based thin film materials required for our solar cell devices are deposited using rf plasma enhanced chemical vapor deposition (PECVD) process using an ultrahigh-vacuum, multi-chamber, load-locked deposition system, as shown in Figure 3.1.2. There are two deposition chambers in this system, with one (Chamber 2) designated for growth of a-Si and a-SiGe intrinsic materials, and the other (Chamber 1) designated for the growth of n-type a-Si and p-type microcrystalline silicon (μc-Si) layers.

Mixtures of Si_2H_6 (Si_2H_6 and GeH_4) and H_2 are used for the deposition of a-Si (a-SiGe) materials. Mixtures of BF_3 (PH_3), SiH_4 and H_2 are used for the deposition of p-type μc-Si (n-type a-Si) layers to form the a-Si n-i-p junctions. 4"x4" stainless steel foils, 0.13 mm thick, with and without a textured Ag/ZnO back-reflector coating, are used as substrates for the solar cell fabrication. Since we deposit both n-layer and p-layer materials in Chamber 1, we pre-coat the chamber under typical p-layer growth conditions for 5 min before substrates are moved in for the p-layer growth.

ITO layers, serving as the top electrodes and anti-reflective coatings, are deposited in an rf sputtering chamber from an In_2O_3/SnO_2 target with 90%/10% composition. In addition, targets with 5% and 15% SnO_2 composition have also been explored. Aluminum grids are evaporated in vacuum at room temperature to improve the current collection.

Current-Voltage characteristics and quantum efficiency curves are measured at UT and at ECD to evaluate solar cell performances.

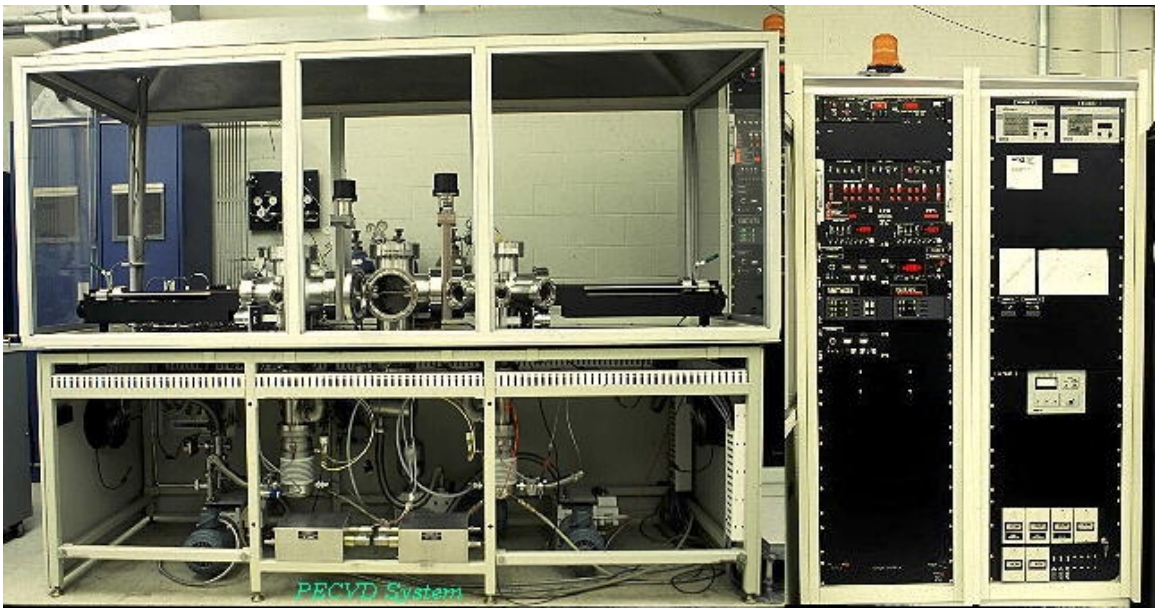

Figure 3.1.2 UT's multi-chamber, loaded-locked, PECVD system used for the a-Si solar cell fabrication.

3.2 Wide Bandgap a-Si Top Cells

The top cell catches blue portion of the solar spectrum. It is crucial that the top cell has good blue response, exhibits high V_{oc} and high FF. The thickness of the top cell is determined by the device requirement of the middle and bottom a-SiGe cells since all three component cells are connected in series in a triple cell. The device structure of a typical top cell is depicted in Figure 3.1.1(a). SS substrates with and without Ag/ZnO back-reflector are used.

Before we discuss the i-layer deposition, we would like to first describe the deposition of doped layers, in particular, the p-layer, which are required for the device operation. Both the n-type and p-type layers are deposited in Chamber 1 which is designated for the deposition of

doped layers. The a-Si n-layer is grown using a gas mixture of SiH_4, PH_3 and H_2 and other deposition conditions including relatively low H dilution and low rf power. The μc-Si p-layer deposition conditions are described in Section 3.2.1.

3.2.1 Optimization of p-layer

Boron doped μc-Si p-layers are used in our a-Si solar cell devices. Compared with their amorphous counterparts, μc-Si p-layers are believed to offer the advantage of a higher V_{oc} and a higher transmission [3.6]. At the beginning, we performed an initial survey study of the p-layer deposition conditions, covering rf power, deposition temperature, gas mixture, deposition time and pressure, and obtained preliminarily optimized deposition conditions. As an example, we show in Table 3.2.1 a series of samples having p-layers with different thicknesses (deposition times). As one can see from the table, V_{oc} was generally higher when the p-layer was thicker (up to a certain thickness) while J_{sc} was generally higher when the p-layer was thinner. The significantly low FF and high R_s for GD86 and GD89 could be partially due to a poorer ITO. A 2min deposition for the p-layer offered a reasonably good V_{oc} and J_{sc} and was therefore selected as a standard deposition time for our baseline samples. Figure 3.2.1 is a J-V curve of a single cell with a preliminarily optimized p-layer.

It has been argued that the device V_{oc} depends sensitively on the buffer layer between the absorber and doped layers [3.7]. In particular, a buffer layer without a band alignment for minority carriers and with a band alignment for majority carriers was suggested to improve V_{oc} since such a buffer layer would block the minority carriers to the contact and allow for reasonable flow of majority carriers [3.7]. We plan to test different buffer layers at the p-i interface to study the dependence of V_{oc} on the band offset of these buffer layers.

Table 3.2.1 Device performance of single junction solar cells having p-layers with different thicknesses.

Sample ID	Time min	V_{oc} V	J_{sc} mA/cm^2	R_s Ω cm^2	FF	P_{max} mW/cm^2
GD89	6	0.951	9.64	37.8	0.569	5.21
GD86	4	0.963	9.94	48.1	0.569	5.45
GD87	2	0.910	10.97	14.4	0.668	6.66
GD88	1	0.878	10.27	8.0	0.721	6.50

Beside the device performance, another critical issue related to the p-layer deposition is the uniformity. We initially observed a serious non-uniformity in the p-layer for samples of 4"x4" size. Therefore, we made a large number of depositions of μc-Si p-layer under different conditions to improve the uniformity yet without causing a loss in our solar cell device performance. We observed that in general the uniformity improved when the deposition pressure was reduced. However, when the pressure was too low, the quality of our devices appeared to suffer. We found that a pressure of 1 Torr was a good compromise for both high uniformity and the high quality for the deposition conditions and chamber geometry that we used.

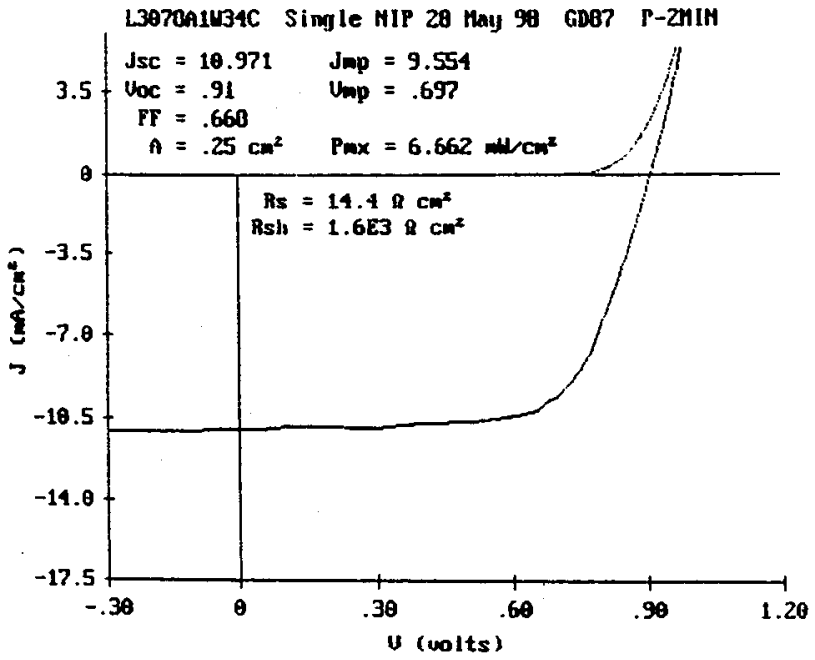

Figure 3.2.1 J-V curve of a single cell with 2min p-layer, deposited on bare SS without backreflector.

3.2.2 Optimization of a-Si intrinsic layer deposition

The a-Si intrinsic layers for the top cells are deposited using Si_2H_6 that is heavily diluted in H_2. Si_2H_6 is used here for the i-layer deposition for the sake of convenience since Si_2H_6 is required for the uniform deposition of a-SiGe. Some time ago, the electrode spacing and the deposition pressure were adjusted and optimized to achieve ease of striking a plasma and deposition uniformity. Currently, the electrode gap is fixed at 2.5 cm and the chamber pressure during deposition is maintained at 0.6 Torr for the standard i-layer deposition condition. The chamber for the i-layer deposition has never been used for the growth of any doped materials. It is not exposed to the air under routine operation. The substrate loading is done through the loading chamber. Separate gas lines are used for the intrinsic chamber and doped chamber to avoid cross contamination. Before the deposition takes place, the chamber is pumped using turbo molecular pump to reach a baseline pressure of 10^{-8} Torr.

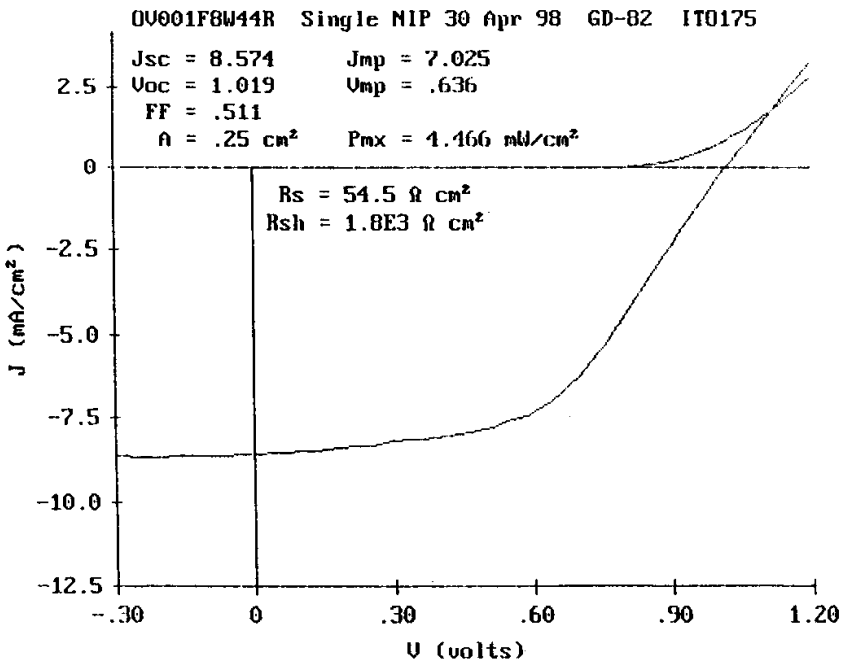

Figure 3.2.2 J-V curve of a single cell with i-layer deposited under high H dilution, showing 1.02 V open circuit voltage.

High open circuit voltage is an important characteristic for the top cell. We varied the conditions of H dilution and deposition temperature to improve solar cell V_{oc}. As a result, we achieved a-Si top cell devices with a V_{oc} up to 1.02 V. Figure 3.2.2 shows an J-V curve of such devices. Unfortunately, the FF for this device is very poor, making it unacceptable for incorporation into a high efficiency device. Deposition conditions for cells with both high V_{oc} and high FF have yet to be developed. At this moment, the highest V_{oc} for top cells having FF greater than 70% is 0.98 V.

It has been found that high quality, stable, a-Si materials are deposited before the onset of microcrystalline formation [3.8]. In general, wide bandgap a-Si materials capable of producing high V_{oc} could be achieved using a very high hydrogen dilution and relatively low deposition temperature. To this end, we produced a series of single junction a-Si solar cells with a-Si i-layers deposited at various temperatures and H dilutions. The results are summarized in Table 3.2.2.

Expectedly, at the same substrate temperature T_s, as the H dilution, R ($=H_2/Si_2H_6$), increases, V_{oc} increases. For example, at T_s=200 ^{0}C, V_{oc} increases from 0.936 V for R=50 to 0.971 V for R=200. For the same dilution level, for example R=100, V_{oc} increases at lower temperature, till the temperature decreases down to a certain level, such as 175 ^{0}C. To avoid the formation of microcrystals in the i-layer, the deposition temperature was reduced while R was increased. In this way, the materials deposited are near the border line of microcrystalline formation yet were still amorphous. For samples deposited at 250 ^{0}C, a R=200 H dilution seems

to be excessive as we see for sample GD300, of which the FF decreased. However, at lower temperature, higher H dilution is needed to maintain high FF. It should be pointed out here that the lower FF in GD290 is likely to be partially due to the increased thickness and partially due to the slightly poorer ITO.

The thickness of an i-layer is measured using a capacitance measurement. The deposition rate is calculated from the i-layer thickness and the deposition time. Figure 3.2.3 shows the deposition rate as a function of the H dilution level, showing that the deposition rate decreases monotonically with the increased H dilution, as expected.

Table 3.2.2 Deposition conditions (substrate temperature and H dilution R) for the i-layers of a series of single junction solar cells.

Sample	T_S	R	d	dep rate	V_{oc}	J_{sc}	FF
	(^{0}C)	(H_2/Si_2H_6)	(nm)	(A/s)	(V)	(mA/cm^2)	(%)
gd279	300	30	185	0.77	0.913	9.9	70.3
gd288	250	40	207	0.69	0.931	11.2	71.1
gd290	250	50	215	0.6	0.926	10.3	66.2
gd299	250	100	172	0.35	0.95	9.7	71.6
gd300	250	200	170	0.24	0.948	7.4	66.3
gd289	200	50	186	0.52	0.936	9.1	72.1
gd291	200	66	189	0.51	0.944	8.9	73.0
gd292	200	100	195	0.41	0.951	9.1	71.8
gd298	200	200	153	0.21	0.971	8.1	70.3
gd293	175	66	201	0.48	0.948	8.9	73.3
gd304	175	100	156	0.33	0.98	9.7	71.1
gd294	175	200	160	0.22	0.966	6.8	71.3
gd295	150	200	159	0.21	0.972	6.4	69.6
gd296	125	200	162	0.22	0.973	5.0	69.8

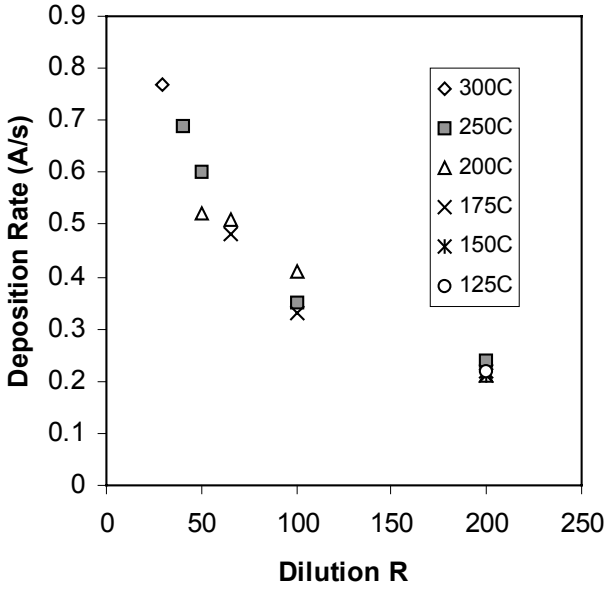

Figure 3.2.3 Deposition rate of the a-Si intrinsic layer as a function of H dilution factor R.

3.3 Mid Bandgap a-SiGe Cells

In the area of mid bandgap solar cells, we deposited many devices with the a-SiGe absorber layers having moderate amounts of Ge. The amount of Ge optimal for the mid-bandgap depends on many factors including the bandgap of the bottom cell. This is due to the constraints in the short circuit current of component cells in a triple-junction, two-terminal structure in which all component cells are connected electrically in series.

The middle cell i-layer is deposited in Chamber 2. The doped layers are the same as those discussed above for top cell. Unlike the top cell structure, as shown in Figure 3.1.1(a), the middle cell i-layer is sandwiched between two a-Si buffer layers. In this way, the material that is in direct contact with the doped layers is intrinsic a-Si that is likely to be of higher quality than a-SiGe. One might worry about the band edge discontinuity between these a-Si buffer layers and the a-SiGe absorber layer. We inserted another a-SiGe buffer layer with a graded bandgap to reduce or eliminate this discontinuity. However, our preliminary results show that such additional bandgap-graded buffer layer does not improve device performance for middle component cells. For *narrower* bandgap a-SiGe absorber layer (for the bottom cell), as to be discussed in Section 3.4.2, a bandgap-graded a-SiGe buffer layer, inserted between an a-Si buffer layer and the a-SiGe absorber layer to eliminate the band edge discontinuity, appears to improve the device performance.

In Table 3.3.1, we show the results of some mid bandgap solar cells with the i-layer deposited with different gas mixtures and different H dilutions. Since the earlier measurements had large scattering, the data listed in Table 3.3.1 are the IV performance measured again a few months after the samples were completed. The FF values are somehow lower than the measurements taken as-deposited. The thicknesses of the i-layers for these devices were measured using capacitance technique. Due to the texture in the back-reflector, the thickness for

samples on back-reflector, GD249-GD251, are underestimated. As we see from the table, when GeH_4 concentration increases in the gas mixture, V_{oc} decreases and J_{sc} increases. GD285 and GD286, although with more GeH_4 than GD249-251, show higher FF. This is due to their i-layers being thinner (note that the thickness values for GD249-251 listed in Table 3.3.1 are underestimated). Compared with GD286, GD302 and GD303 were deposited with more GeH_4 and with a higher R. The reduced bandgap due to a higher Ge content is partially offset by the slight widening of bandgap due to the higher R, resulting in no noticeable change in V_{oc}.

In general, the results of this set of middle cells show large fluctuations thus clear conclusions are hard to draw. After the fabrication of these sets of samples, the reproducibility in both the fabrication and measurement have been improved. We plan to repeat this set of samples to gain a better picture of middle cell performance.

Table 3.3.1 J-V performance of a-SiGe middle cells with i-layer deposited with different GeH_4/Si_2H_6 gas ratio and under different H dilution.

Sample	ratio	R	Ge grading	d	V_{oc}	FF	J_{sc}	With BR ?
	(GeH_4/Si_2H_6)	(H_2/Si_2H_6)		(nm)	(V)	(%)	(mA/cm^2)	
GD249	0.18	40	no	233	0.885	53.4	14.7	Yes
Gd250	0.24	40	no	190	0.858	53.9	17.5	Yes
GD251	0.29	40	no	210	0.840	54.3	20.0	Yes
GD286	0.36	40	no	195	0.811	60.6	13.1	No
GD285	0.36	40	yes	216	0.799	59.2	14.0	No
GD302	0.40	50	no	183	0.797	57.4	12.4	No
GD303	0.40	66	no	169	0.794	52.7	11.7	No

3.4 Narrow Bandgap a-SiGe Cells

Narrow bandgap a-SiGe solar cell research is one of the main thrusts of this program. In this section, we will describe our research in the following areas.

a. a-SiGe solar cells with different Ge content
b. effect of bandgap graded buffer layer on the device performance
c. a-Ge solar cells

3.4.1 a-SiGe Solar Cells with Different Ge Content

A high-quality narrow-bandgap material is critical to the achievement of high efficiency triple-junction solar cells. We have studied the deposition of a-SiGe solar cells with different bandgaps. Table 3.4.1 summarizes the results for three a-SiGe samples deposited on Ag/ZnO back-reflectors. The i-layers in all of these devices have graded bandgaps to enhance hole collection. In reference to the standard a-SiGe device which was used for the fabrication of an earlier 9.7% triple junction solar cell, we investigated a-SiGe cells with approximately 15% more GeH_4 and 15% less GeH_4 in the gas mixtures.

The data in the J_{QE} column was obtained by integrating the QE curve with AM1.5 global spectrum over the range of our QE measurements (420-900 nm). As we see from Table 3.4.1, when more GeH_4 was added in the gas mixture, V_{oc} and FF decreased while J_{QE} increased. When less GeH_4 was added, V_{oc} increases, without much loss in the J_{QE}. Figure 3.4.1 shows the QE curves for this set of a-SiGe devices. The red response at 800 nm is around 50% for both GD109 and GD110. The low FF for these devices needs to be improved. In addition, this set of samples has large variation in thickness within a 4" by 4" area, causing additional fluctuation in the device performance. The deposition uniformity also needs to be improved.

In Figure 3.4.2, we show the J-V curve for an a-SiGe solar cells with Ge content similar to that of GD110 above but with higher H dilution for the i-layer deposition. It was deposited on a back-reflector. This a-SiGe devices show an initial efficiency of 8.3% with V_{oc} of 0.717 V, J_{sc} of 19.7 mA/cm^2 and FF of 0.589. The improved performance compared with GD110 was due to higher quality i-layer, a better ITO top electrode and that metal grids was evaporated on top for enhanced current collection.

Table 3.4.1. Device data for a series of a-SiGe solar cells having i-layers deposited under different deposition conditions.

Samples	GeH_4/Si_2H_6	thickness (nm)	V_{oc} (V)	J_{QE} from QE (mA/cm^2)	FF	P_{max} (mW/cm^2)
GD109 Standard	0.88	160-280	0.681	19.3	0.530	6.97
GD110 15% more Ge than Std	1.03	190-370	0.634	21.3	0.473	6.39
GD111 15% less Ge than Std	0.78	110-160	0.714	20.0	0.527	7.53

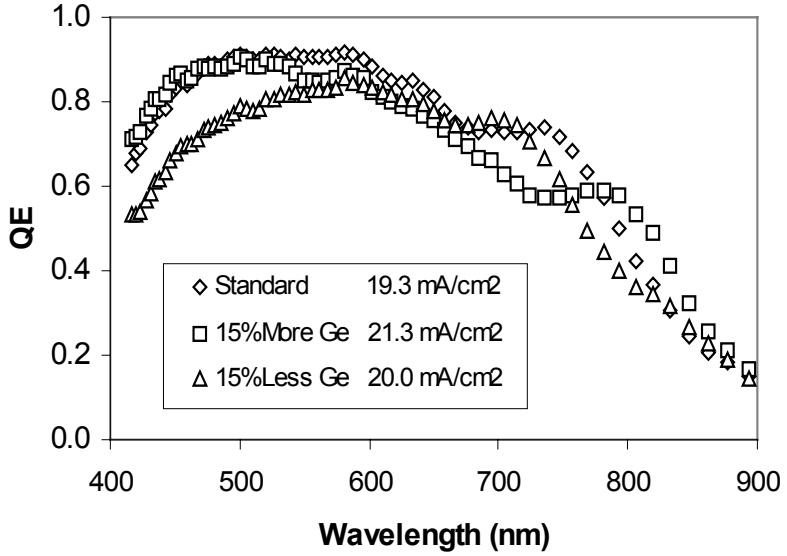

Figure 3.4.1 Quantum efficiency curves of a-SiGe solar cells.

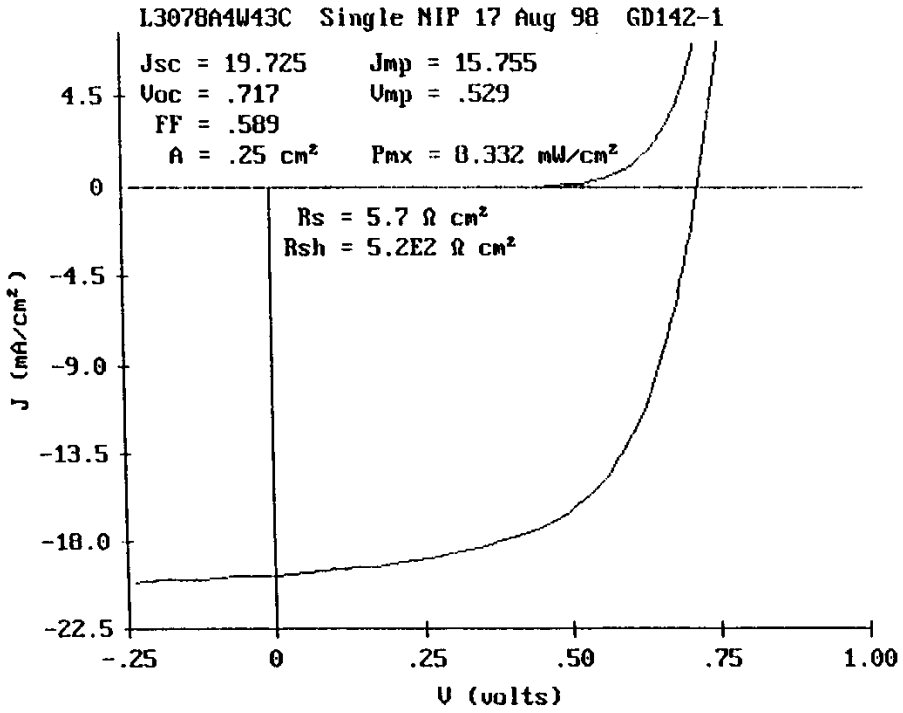

Figure 3.4.2 J-V curve of an a-SiGe solar cell with 8.3% initial efficiency.

3.4.2 Effect of Bandgap Graded Buffer Layer for Narrow Bandgap a-SiGe Cells

Narrow bandgap a-SiGe materials and solar cell devices have been studied extensively for their use in the spectrum splitting, multiple-junction a-Si based solar cells [3.9-3.12]. To achieve high conversion efficiency solar cells, an a-SiGe absorber layer is usually sandwiched between two thin a-Si buffer layers which are in direct contact with the p- and n- doped layers [3.11-3.13]. These a-Si buffer layers were found to enhance the performance of a-SiGe solar cells. However, even with these a-Si buffer layers, there is still an abrupt discontinuity in the bandgap at the interfaces between these buffer layers and the a-SiGe absorber layer. We investigated the effect of inserting additional a-SiGe interface layers between these a-Si buffer layers and the a-SiGe absorber layer. We found that such additional interface layers increased solar cell V_{oc} and FF sizably, most likely due to the reduction or elimination of the abrupt bandgap discontinuity between the a-SiGe absorber layer and the a-Si buffer layers [3.13].

In this section, we report our study on the insertion of additional a-SiGe interface layers (with less Ge compared with the absorber) which reduces the bandgap offset.

The a-SiGe and a-Si materials used in this study were deposited using UT's PECVD system. A gas mixture of GeH_4, Si_2H_6 and H_2 were used for the a-SiGe deposition and Si_2H_6 and H_2 for a-Si deposition. The deposition conditions included a substrate temperature range of 300-400 ^oC, a chamber pressure of 0.5-0.6 Torr and an rf power of 2.5-3.0 W for the a-SiGe and a-Si layer depositions. Different GeH_4 to Si_2H_6 ratios were used to achieve different bandgaps for a-SiGe material. Graded bandgaps for the a-SiGe absorber layer and the a-SiGe buffer layers were achieved by adjusting GeH_4 flows during growth. The GeH_4/Si_2H_6 gas flow ratio for the a-SiGe

absorber layers studied here was 0.68. All of the intrinsic absorber and buffer layers were deposited in Chamber 2.

The device structure used in this study was: SS/Ag/ZnO/n(a-Si)/b(a-Si)/i(NBG a-SiGe)/b(a-Si)/p(μc-Si)/ITO for the standard device and SS/Ag/ZnO/n(a-Si)/b(a-Si)/b(a-SiGe)/i(NBG a-SiGe)/b(a-SiGe)/b(a-Si)/p(μc-Si)/ITO for the new devices under study, where b(a-Si) and b(a-SiGe) are thin a-Si and a-SiGe buffer and interface layers, respectively.

Figure 3.4.3 shows the structure of the various devices used in this study. Fig. 3.4.3(a) is a schematic of the structure for standard a-SiGe devices, showing two a-Si buffer layers on both sides of a-SiGe absorber layer. Fig. 3.4.3(b) and (c) show the schematics of the device structures with the additionally inserted a-SiGe interface layers having a fixed Ge content (Fig. 3.4.3(b)) and with interface layers having a graded bandgap (Fig.3.4.3(c)).

Table 3.4.2 lists the photovoltaic parameters of the open circuit voltage V_{oc}, short circuit current density J_{sc}, fill factor FF and the maximum power output P_{max} of a-SiGe solar cells with different interfacial buffers. The J_{sc} values listed in this table are likely to be overestimated since these J_{sc} values were measured under an ELH lamp which is richer in the red. However, the relative trend is the same. GD180 is a standard a-SiGe device (Fig.3.4.3a) and GD202 contains a-SiGe buffer layers with a fixed Ge content inserted between the a-Si buffers and a-SiGe i-layer at both the n- and p-interfaces (See Fig.3.4.3b), while GD203 and GD209 have Ge-content graded buffer layers at both interfaces (See Fig.3.4.3c). It is clearly seen that the V_{oc} and FF have been increased due to the introduction of the additional a-SiGe interfacial layers and the improvements are approximately in the range of 2-5% for V_{oc} and 5-10% for FF. The V_{oc} and FF enhancement was higher for graded buffer layers. For this reason, the J-V characteristics of GD180 and GD209 are compared in Fig.3.4.4, and the results of these two devices are discussed further in the following.

Figure 3.4.5 shows the QE curves for a-SiGe cells without (GD180) and with (GD203 and GD209) bandgap graded interfacial layers. The spectral responses of these devices are approximately the same in the red region. The small variation in the red could also be due to the variation in the back-reflector. The difference in the blue region of the QE curve mostly resulted from the variation in the transmission of ITO films.

Table 3.4.2 Photovoltaic parameters of solar cells with different buffer layers

Samples	V_{oc} (V)	J_{sc} (mA/cm^2)	FF	P_{max} (mW/cm^2)
GD180 Standard	0.647	23.5	0.506	7.7
GD202 w/ a-SiGe buffer	0.662	21.6	0.534	7.6
GD203 w/ graded a-SiGe buffer	0.680	23.4	0.536	8.5
GD209 w/ graded a-SiGe buffer	0.675	24.3	0.559	9.2

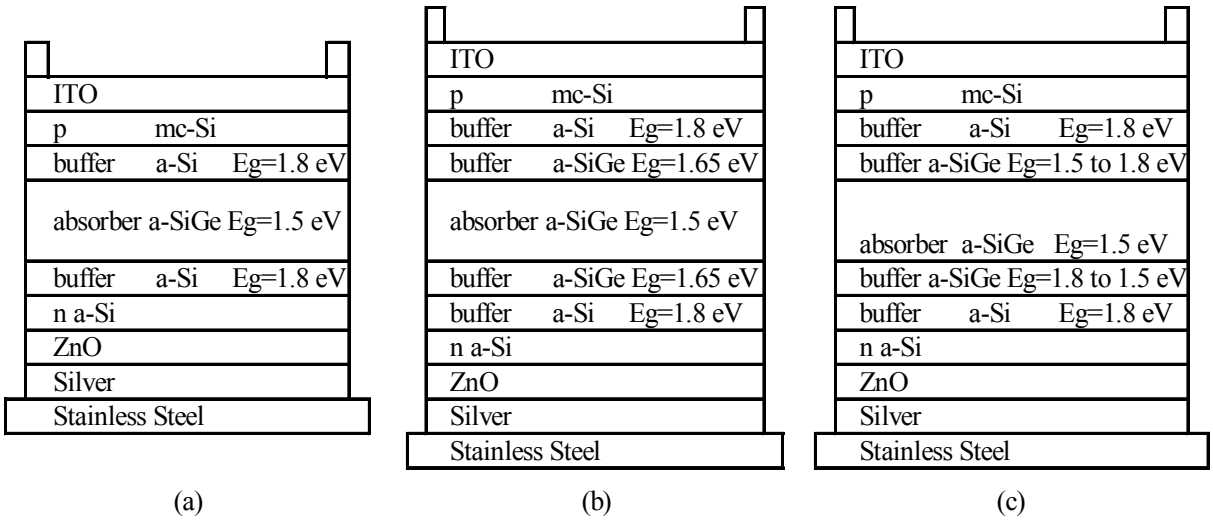

Figure 3.4.3 (a) (b) and (c) Schematic layer structure diagram of a-SiGe solar cells with different interfacial buffer layers.

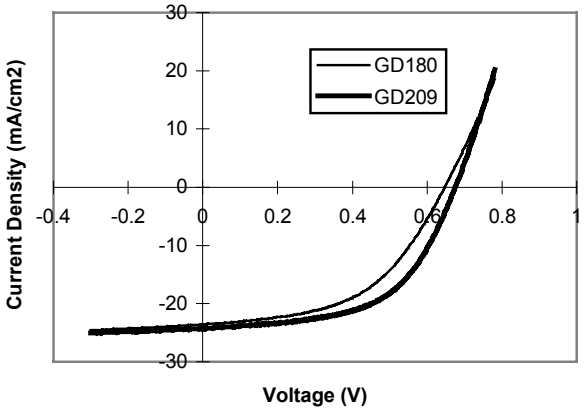

Figure 3.4.4 Illuminated J-V characteristics of GD180 and GD209 samples

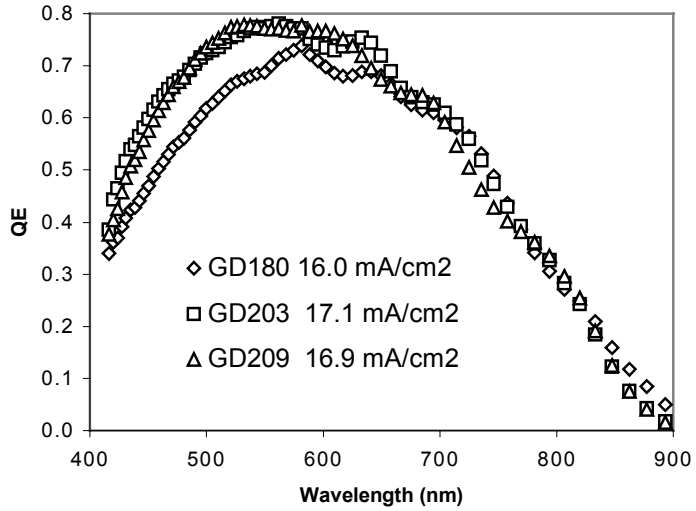

Fig.3.4.5 Quantum efficiency curves of a-SiGe solar cells. GD180 is standard solar cell, while GD203 and GD209 are cells with bandgap graded a-SiGe buffers.

We calculated the current density values, J_{QE}, by integrating the quantum efficiency curves over AM1.5 Global spectrum, as an independent check of the short circuit current values. The obtained J_{QE} and the relative P_{max} calculated from these J_{QE} values are summarized in Table 3.4.3. The J_{QE} value in Table 3.4.3 and the J_{sc} values in Table 3.4.2 are quite different. This is because J_{sc} values in Table 3.4.2 were measured using an ELH lamp. On the relative scale, we find that the short circuit currents of standard a-SiGe sample (GD180) and the a-SiGe samples with graded buffer layers (GD203 and GD209) are approximately the same within the experimental variation. The enhancement in V_{oc} and FF result in a net increase in device P_{max}.

Table 3.4.3 a-SiGe solar cell device performance

Sample	J_{QE} (mA/cm^2)	QE @800nm	V_{oc} (V)	FF	Relative P_{max} (mW/cm^2)
GD180	16.6	0.288	0.647	0.51	5.5
GD203	17.7	0.305	0.680	0.54	6.5
GD209	17.5	0.315	0.675	0.56	6.6

The influences on the performances of the solar cells from the recombination processes taking place at both interfaces between the intrinsic a-SiGe layer and doped layers could also be observed from the ideality factor (n) of the p-i-n devices. The improved J-V performance in the cells with bandgap graded a-SiGe interfacial layers are reflected also in the improvement of the ideality factor and the reduction in the reverse saturation current density (J_o) of these devices.

It is well known that the J-V characteristics of p-i-n a-Si solar cells under illumination can be approximately described by using transport equation of an ideal p-n junction [3.14]:

$$J_{ph} = J_o [\exp(q(V - J_{ph}R_s) / nkT) - 1] - J_{sc} \quad (1)$$

where n is the ideality factor of the device under illumination, J_{ph} represents the photocurrent density, $(V - J_{ph}R_s)$, in which J_{ph} could have negative value, represents the voltage at the junction of an ideal diode. The effect of the equivalent series resistance R_s is included in the equation, while the equivalent shunt resistance R_{sh} is not taken into account. In order to obtain n factor directly from experimental measurement, one could use the dependence of V_{oc} on J_{sc} under varying light intensities,

$$V_{oc} = (nkT/q)(\ln(J_{sc}/J_o + 1)) \quad (2)$$

where the effect of R_s is avoided, hence n factor can be determined from the slope of the V_{oc} versus $\ln(J_{sc})$. Figure 3.4.6 shows the experimental data of J_{sc} (V_{oc}) measured under various light intensities for samples GD180, with the standard structure of a-SiGe bottom cell, and GD209, with a graded a-SiGe buffer layer at both interfaces. It is seen that there is a nearly linear relationship between $\ln(J_{sc})$ and V_{oc} with R-squared values of 0.9975 and 0.9998 for the two samples studied, consistent with the expectation of Eq. (2). From the slopes of these two lines we deduced the quality factor n to be 2.02 and 1.77, for the samples without (GD180) and with (GD209) graded a-SiGe interfacial layers at the p-i and i-n junction between the a-Si buffer layer and a-SiGe intrinsic layer, respectively. The reverse saturation current density, obtained from these fittings, were 8.3×10^{-8} A/cm^2 and 7.2×10^{-9} A/cm^2 for GD180 and GD209, respectively. The reductions in the n and J_o values indicate an improvement in the p-n junction quality and a decrease in the recombination rate of extra minority carriers, as a result of these additional interfacial layers.

In summary, we explored the effect of additional a-SiGe interface layers between narrow bandgap a-SiGe absorber layer and the a-Si buffer layers. The reduction and elimination in the bandgap offset at these interfaces result in sizable increases in device V_{oc} and FF, although the J_{sc} was somewhat unchanged.

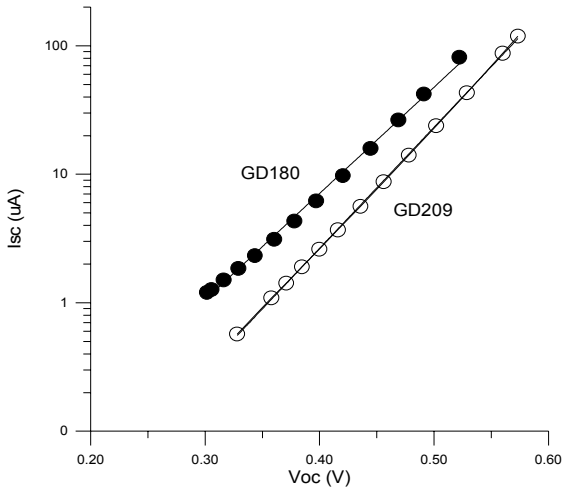

Fig.3.4.6 I_{sc} versus V_{oc} under various light intensity for samples GD180 (solid circle) and GD209 (open circle)

3.4.3 a-Ge solar cells

We deposited solar cells with hydrogenated amorphous germanium (a-Ge) as the absorber layer. The motivation is to find out its suitability for applications that require high current densities. GeH_4 gas diluted in H_2 is used as the precursor for the a-Ge i-layer deposition. Doped layers identical to those mentioned above were used. Thin a-Si buffer layers were inserted between the a-Ge and doped layers.

Figure 3.4.7 shows the J-V curve for a representative a-Ge solar cell. The V_{oc} and FF are low. Such a-Ge material is not suitable as solar cell absorber layer, but could be considered for use in other devices that operate under reverse bias.

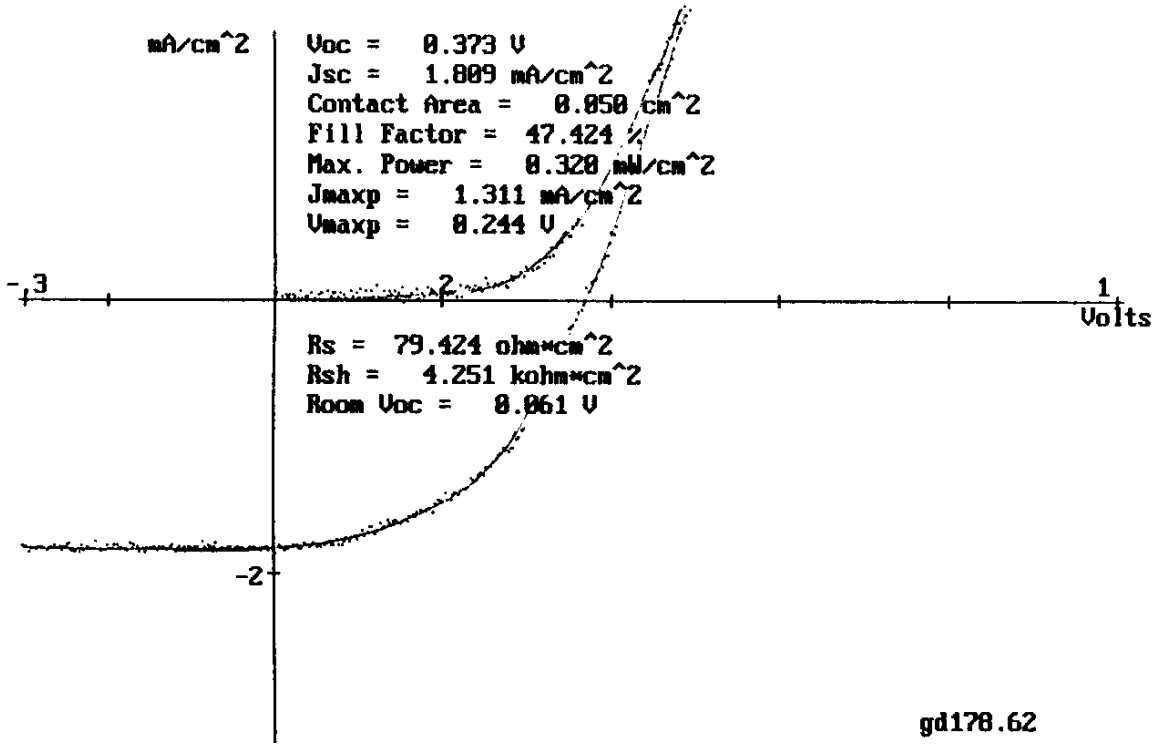

Figure 3.4.7 J-V curve for a representative a-Ge solar cell.

3.5 Fabrication of Triple-Junction Solar Cells

We have fabricated several series of triple-junction a-Si/a-SiGe/a-SiGe solar cells, having a structure shown in Figure 3.1.1(b). The back-reflector coated stainless steel substrates were provided by ECD. The middle and bottom cell i-layers are a-SiGe alloys with different amounts of Ge content. The bottom cell a-SiGe layer has a graded bandgap to enhance hole collection.

Figure 3.5.1 is the J-V curve for a triple cell produced in our lab during the second quarter of this Year1 program. The initial efficiency for this triple was 9.7%, which was improved from our previous 8.4%.

We incorporated the improvement in the bottom and top cells into triple-junction a-Si based solar cells. Figure 3.5.2 is a J-V curve for such a triple-junction solar cell measured at ECD under a solar simulator light, showing a 10.6% initial efficiency. Figure 3.5.3 is the QE curve for the triple-cell measured at ECD. The short circuit current value J_{QE} was obtained by integrating the QE spectrum over AM1.5 global spectrum. For this triple-cell (GD218-1), the short circuit current for the component cells are: 7.54, 6.85 and 9.24 mA/cm^2 for the top, middle and bottom cells, respectively. The total current is 23.6 mA/cm^2. The triple-cell current seems to be limited by the middle component cell. This limiting current (6.85 mA/cm^2) is the same, within experimental error, as we measured from the J-V curve (6.76 mA/cm^2) indicating that the QE and the J-V curves are consistent with each other for this device.

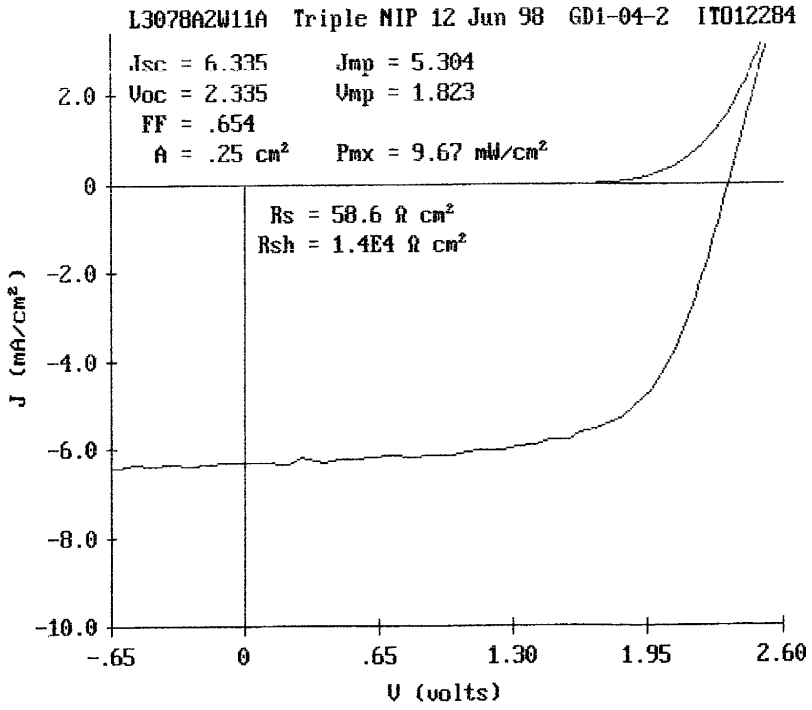

Figure 3.5.1 J-V curve for a triple cell achieved during the second quarter of this Year1 program.

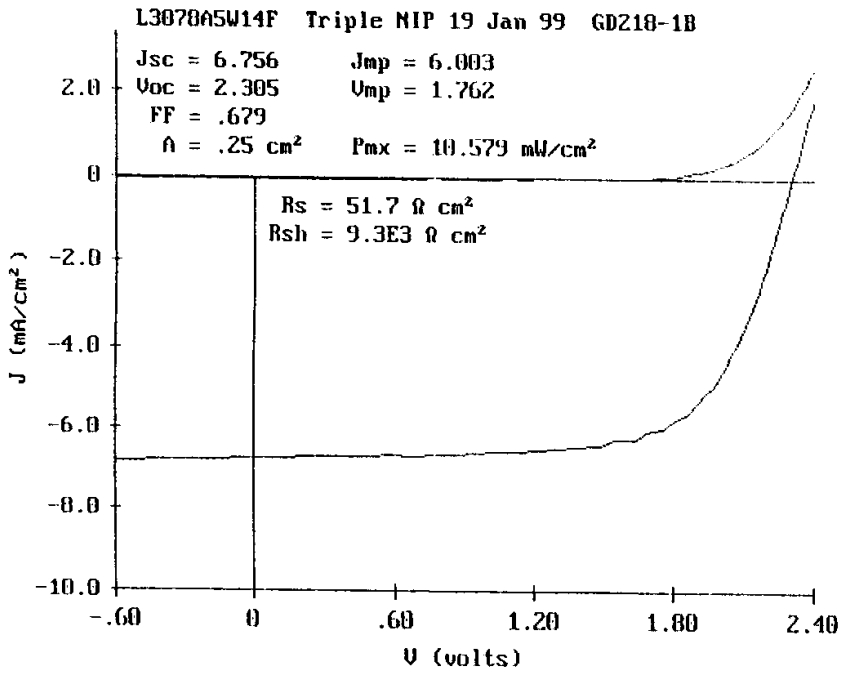

Figure 3.5.2 J-V curve of an improved triple-cell, showing 10.6% initial efficiency.

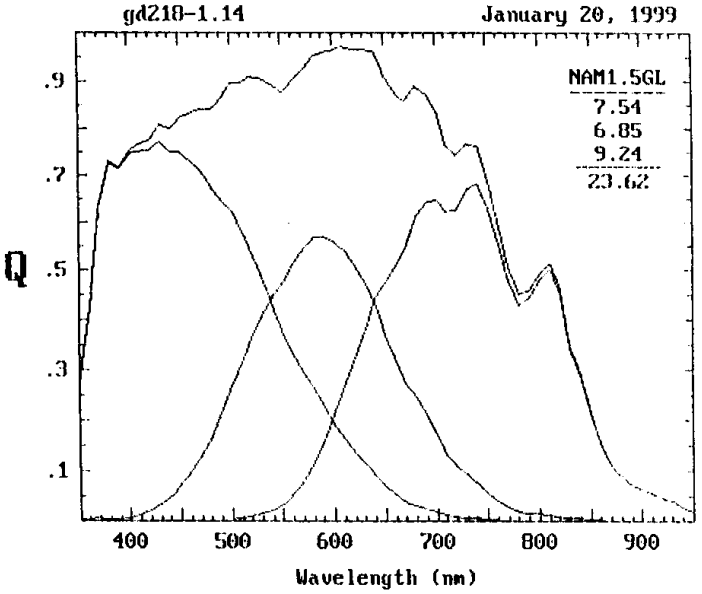

Figure 3.5.3 QE curve of the 10.6% triple-cell, showing a 23.6 mA/cm^2 total current.

Table 3.5.1 shows the J-V performance for a series of triple-junction devices having different top cell i-layer thickness. Some of the cells show a P_{max} of around 11%. This is most likely caused by the underestimate of the actual active area of the device due to the fuzzy ITO. Sample GD218 is reliable since the ITO is not fuzzy. In addition, its J_{sc} value agrees well with the J_{QE} calculated from QE curves.

Samples GD218 and GD219 were light soaked under one sun light intensity at approximately 50 ^{0}C for 1166 hours. Light degradation of representative samples is also shown in Table 3.5.1. After light soaking, Device GD218-1#14 seems to be shunted. However, from the relative degradation of GD219 cells which show degradation of 6.4% and 12%, we estimate that the degraded efficiency of GD218 would be from 9.3% to 9.9%, had it not been shunted during the light soaking.

When the J-V curve of a triple cell is measured under red-rich light, the top cell is severely mismatched. The FF of the triple cell under red light reflects the FF of the top cell. Figure 3.5.4 shows the J-V curve of triple-cell GD219 measured under red light showing a high FF of 0.80. This suggests that our top cell is of high quality.

In summary, incorporating the improvements that we made recently, we fabricated triple-cells with 10.6% initial efficiency and around 9-10% stable efficiency after 1166 hours of one sun light soaking.

Table 3.5.1 Performance of triple-junction solar cells before and after 1166 hours of 1 sun light soaking at 50 ^{0}C.

Device No.	LS time (hours)	V_{oc} (V)	J_{sc} (mA/cm^2)	FF	R_s ($\Omega \bullet m^2$)	Area (cm2)	Efficiency (%)	Degrad. (%)
218-1#14	0	2.305	6.76	0.68	51.7	0.25	10.58	--
	1166	2.270	6.51	0.53	114	0.25	7.86	25.7
219-1#32	0	2.277	7.76	0.63	65.6	0.25*	11.10	--
	1166	2.251	7.67	0.60	69.3	0.25*	10.39	6.4
219-1#33	0	2.291	7.67	0.66	50.7	0.25*	11.57	
	1166	2.254	7.46	0.61	66.1	0.25*	10.18	12.0

* Area may not be accurate.

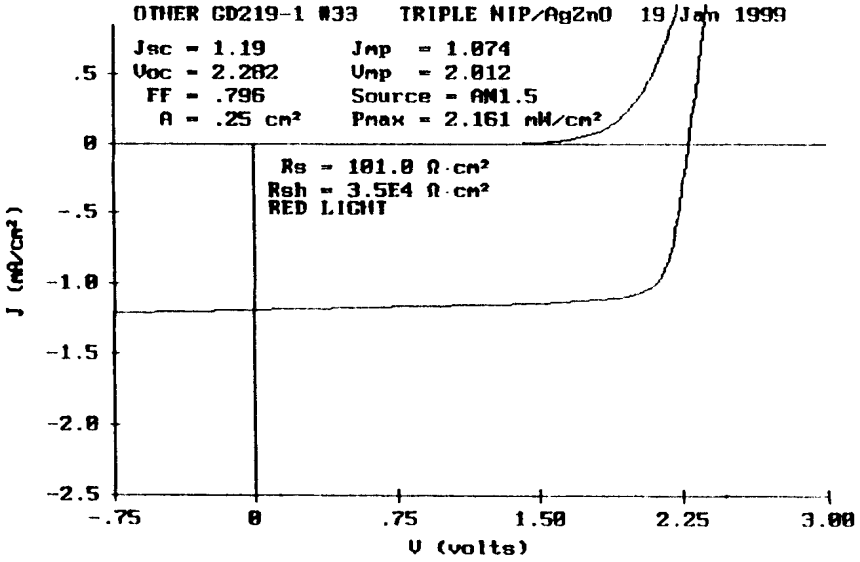

Figure 3.5.4 J-V curve of a triple-cell showing 0.80 fill factor when measured under red-rich light.

3.6 Sputter Deposition of ITO

Indium tin oxide (ITO) films used for a-Si solar cells have been deposited using evaporation and sputtering [3.15-3.18]. We have studied ITO sputter deposition for use in a-Si n-i-p solar cells. The ITO films were deposited using RF sputtering from a 2" sputter gun in a vacuum chamber backed by a turbo molecular pump. The sputter sources used in this study were In_2O_3/SnO_2 targets having a In_2O_3 content of 95, 90 and 85%, respectively. In searching for the optimal ITO film properties, we have investigated a broad deposition parameter space including RF sputtering power, substrate temperature, and Ar pressure. The ITO films were deposited either on glass substrates for resistivity and transmission measurements, or on a-Si n-i-p solar cells for J-V and quantum efficiency measurements.

Table 3.6.1 lists the various sputter deposition conditions for a series of ITO films deposited in 30 min. In this table, the film thickness, d, was calculated from the interference fringes in the optical transmission. R_{sh} is the sheet resistance of the film, measured using a four point probe. T is the transmission around 550 nm, calculated using $T=(T_{max} \bullet T_{min})^{1/2}$, where T_{max} and T_{min} are the transmission maximum and minimum in the UV/Visible transmission spectroscopy. Since the desirable ITO thickness in an a-Si solar cell is around 65 nm to achieve antireflection, we calculated an *effective* sheet resistance (R*) for a film which would have been 65 nm thick using

$$R^* = R_{sh} \cdot \frac{d}{65nm} \qquad (3)$$

In addition, we calculate the absorption coefficient, α, of ITO films using

$$T = \frac{(1-R_1)(1-R_2)\exp(-\alpha \cdot d)}{1-R_1 R_2 \exp(-2\alpha \cdot d)} \qquad (4)$$

where R_1 and R_2 are the reflectances at the interfaces with air and glass, respectively, with $R=\{(n_1-n_2)/(n_1+n_2)\}^2$. Refractive indices of 1 and 1.5 are used for air and the glass substrates. Since the refractive index for ITO varies with wavelength near 550 nm, we used 2.1 as the ITO refractive index in our calculation of R_1 and R_2. From Eq.4, we obtained the absorption coefficient and then used it to calculate an *effective* absorption loss (A*) for an ITO film that would have been 65 nm thick using

$$A^* = 1-\exp(-\alpha \cdot 65nm) \qquad (5)$$

The values of R* and A* therefore reflect the film performance of the ITO layers.

Figure 3.6.1 shows the dependence of the film thickness on RF power. The film thickness increases linearly with the increased RF power, independent of temperature and pressure within the selected ranges. Figure 3.6.2 shows R* as a function of RF power at various temperatures and chamber pressures. To limit the ITO electrical loss to less than 1% at the maximum power point of a triple-junction a-Si solar cell, we need an ITO sheet resistance of less than ~80 Ω/□, or the resistivity (ρ) to be lower than $\sim 5\times10^{-4}$ Ω•cm for a 65 nm thick ITO film.

Table 3.6.1 Deposition conditions and quality for ITO films deposited under various sputtering conditions.

Sample No.	RF (W)	Temp (C)	P (mT)	d (nm)	Rsh (Ohm)	T (%)	R* (Ohm)	A* (%)
ITO-37	30	225	8	454	1.5E+ 01	83.3	1.1E+ 02	0.47
ITO-25	40	225	8	620	5.9E+ 00	80.2	5.7E+ 01	0.75
ITO-34	50	225	8	779	5.0E+ 00	80.2	5.9E+ 01	0.60
ITO-50	10	150	6	171	1.9E+ 02	80.0	5.1E+ 02	2.77
ITO-49	20	150	6	327	4.2E+ 01	81.9	2.1E+ 02	1.00
ITO-47	30	150	6	449	2.4E+ 01	81.0	1.7E+ 02	0.89
ITO-48	40	150	6	601	1.5E+ 01	79.6	1.4E+ 02	0.85
ITO-55	50	150	6	771	1.1E+ 01	79.7	1.3E+ 02	0.65
ITO-66	60	150	6	916	2.4E+ 01	79.2	3.4E+ 02	0.60
ITO-51	10	175	6	176	2.2E+ 02	80.0	6.1E+ 02	2.70
ITO-53	30	175	6	460	1.8E+ 01	80.8	1.2E+ 02	0.90
ITO-67	50	175	6	785	2.3E+ 01	76.6	2.8E+ 02	0.97
ITO-68	30	200	6	452	3.1E+ 01	79.9	2.2E+ 02	1.08
ITO-69	40	200	6	589	1.3E+ 01	81.1	1.2E+ 02	0.66
ITO-71	50	200	6	761	1.1E+ 01	80.1	1.3E+ 02	0.62
ITO-72	30	225	6	459	1.8E+ 01	81.0	1.3E+ 02	0.87
ITO-73	40	225	6	547	8.8E+ 00	80.5	7.4E+ 01	0.80
ITO-65	20	250	6	288	2.1E+ 01	80.8	9.5E+ 01	1.44
ITO-75	30	250	6	378	8.7E+ 00	82.8	5.1E+ 01	0.67
ITO-78	40	250	6	586	1.1E+ 01	80.2	9.8E+ 01	0.79
ITO-79	50	250	6	760	9.6E+ 00	79.4	1.1E+ 02	0.70
ITO-16	30	200	18	387	1.4E+ 03	84.0	8.1E+ 03	0.41
ITO-20	20	225	18	266	1.4E+ 04	83.9	5.7E+ 04	0.63
ITO-24	30	225	18	386	7.0E+ 03	85.1	4.1E+ 04	0.19
ITO-19	40	225	18	606	1.3E+ 02	83.8	1.2E+ 03	0.29
ITO-23	50	225	18	741	1.0E+ 02	82.8	1.2E+ 03	0.34
ITO-14	30	250	18	940	8.9E+ 02	85.0	1.3E+ 04	0.09
ITO-15	30	250	18	320	1.5E+ 03	85.0	1.1E+ 04	0.26

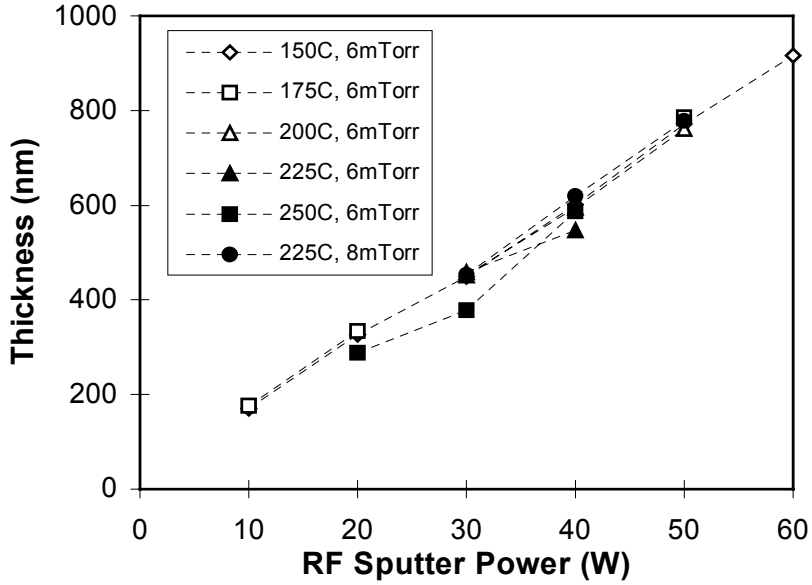

Figure 3.6.1 Thickness of ITO films as a function of the rf power.

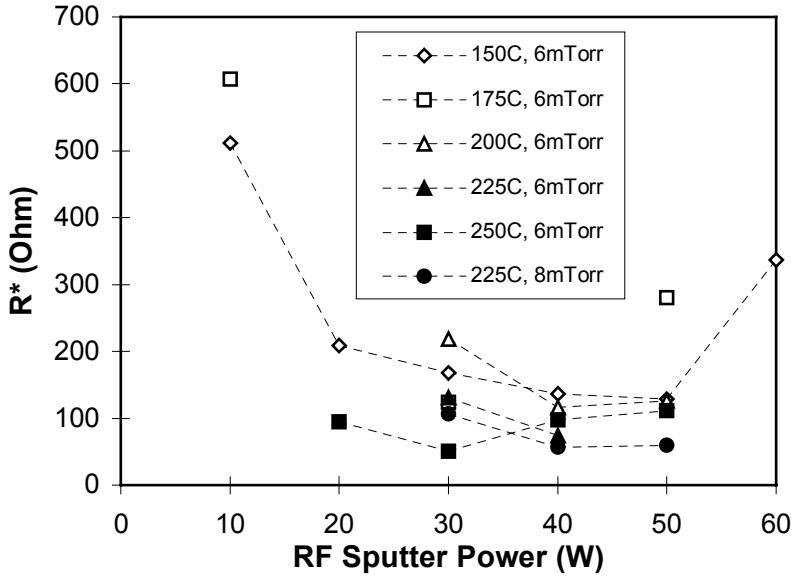

Figure 3.6.2 Effective sheet resistance R* as a function of rf power for various temperature and Ar pressure.

From Figure 3.6.2, we observe that only those ITO films deposited at or above 225 ^{0}C and with RF power around 30-50 W could meet $\rho \leq 5\times10^{-4}$ Ω•cm requirements. At temperatures lower than 200 ^{0}C, the resistivity is too high.

Figure 3.6.3 shows the effective absorption A* for different RF power under various temperatures and pressure conditions. Again, to have the absorption loss lower than 1%, we will need to have a minimum sputtering power of around 30 W.

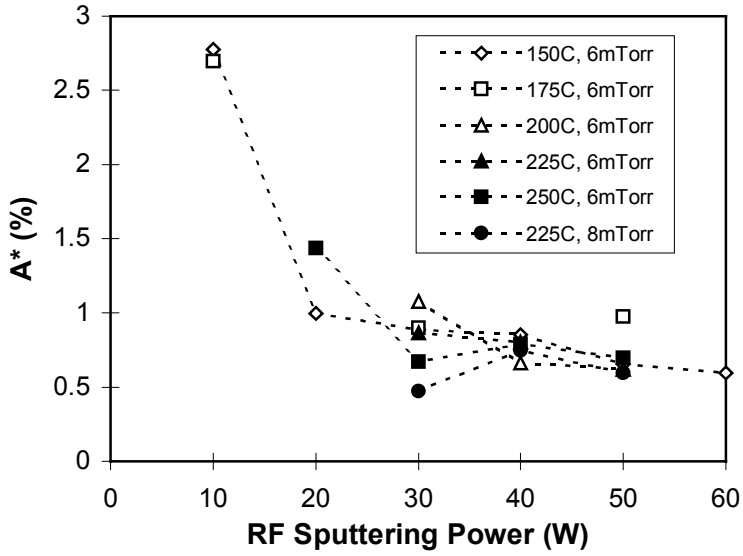

Figure 3.6.3 Effective absorption A* of ITO films as a function of rf power for various deposition temperature and Ar pressure.

Among all the deposited ITO films, those made under conditions of RF power within 30-50W, temperature within 225-250 ^{0}C and pressure around 6-8 mTorr demonstrate the optimal film properties: R^*=50 Ω and A^*<1%. This range of conditions was then used as a starting point for the study of ITO films on substrate-type a-Si solar cells in which an ITO film intimately contacts a μc-Si p-layer.

We deposited approximately 65-75 nm thick ITO films on a-SiGe solar cells prepared on bare stainless steel without the use of a back-reflector. Three different sputtering targets having different In_2O_3 and SnO_2 concentrations were used. In Table 3.6.2, we list the device data for three a-SiGe solar cells with their ITO layers deposited using different targets. Again, the 90/10 target provides the highest FF and J_{sc} among the three samples, suggesting that the 90%/10% In_2O_3/SnO_2 target might be more desirable for use in a-Si based substrate-type solar cells. We would like to point out that these preliminary results were obtained from limited samples and show large fluctuations. Further study is needed to draw a general conclusion.

Table 3.6.2 J-V data of solar cells with ITO deposited from In_2O_3/SnO_2 targets having different compositions.

Sputter Target In_2O_3%/SnO_2%	V_{oc} (V)	J_{sc} (mA/cm^2)	FF	R_s (Ω•cm^2)	P_{max} (mW/cm^2)	J_{QE} from QE (mA/cm^2)
95/5	0.71	11.8	0.46	28	3.9	11.6
90/10	0.69	13.5	0.55	22	4.3	12.2
85/15	0.65	10.5	0.41	35	2.8	10.6

In summary, good quality ITO films were sputter-deposited for use as the top electrodes of substrate-type a-Si based solar cells. The ITO films, deposited at elevated temperature (225-250 ^{0}C) and low pressure (~8 mTorr) with an RF power of 30-50 W in a 2" sputter gun, exhibit an effective sheet resistivity of approximately 50 Ω and absorption loss of less than 1%. In our preliminary study, ITO films deposited using 90%/10% In_2O_3/SnO_2 target show higher performance than 95%/5% and 85%/15% ITO targets when being used in a-Si alloy solar cells.

3.7 Outside research collaborations

We have collaborated with several outside research groups during this reporting period. We fabricated a-SiGe devices for Prof. Daxing Han at U. of North Carolina and Prof. Rubin Braunstein at UCLA. They have measured electroluminescence and mobility-life time properties of our devices, respectively. Those results will be reported in their annual reports.

In addition, we have deposited two series of samples for collaboration with Prof. Y. H. Kao at SUNY-Buffalo. One group of samples were made with different amounts of Ge while the other group of samples were deposited with different amounts of H-dilution. The Buffalo group is studying the interface properties of thin a-Si and a-SiGe based samples.

3.8 Conclusions/Future Directions/Acknowledgments

During the first program year, we have performed all of the tasks previously planned. We have studied and optimized the fabrication of top, middle and bottom component cells, as well as non-semiconductor layers such as ITO top electrodes. We have improved our baseline triple-cell fabrication from 8.4% to 10.6% (initial efficiency).

The following is a list of studies that we plan to do in the near future:

- further improvement in triple-cell fabrication
- hot-wire deposition of high quality a-SiGe intrinsic materials at high rate for use as the narrow bandgap absorber layer;
- stability study of a-Si alloy materials and devices and the comparison of light soaking degradation in thin film materials and solar cell devices;
- measurement of component cell I-V curves in a triple stack;
- further optimization of sputter deposition of ITO films; and
- further improvement of the i-layer quality and light stability.

We would like to thank Dr. Pratima Agarwal (Postdoc) for helps in preparing this report. Helps from our colleagues at ECD and United Solar, in particular from Mr. T. Liu, Dr. S. Jones, Dr. J. Yang and Dr. S. Guha, are deeply appreciated. We thank the members of the National a-Si Teams for valuable comments and discussions and thank Dr. D. Han of Univ. of North Carolina, Dr. R. Braunstein of UCLA, and Dr. Y. H. Kao of SUNY-Buffalo for collaborations. We are especially grateful to NREL for support and to Bolko von Roedern, our contract monitor for his support and advice.

3.9 References

[3.1] J. Yang, A. Banerjee, S. Sugiyama, and S. Guha, Proc. of 2nd world Conference on Photovoltaic Solar Energy Conversion, Vienna, Austria, 6-10 July 1998.

[3.2] J. Yang, A. Banerjee, and S. Guha, in Proc. of NREL/SNL Photovoltaic Program Review Meeting, Nov. 18-22, 1996, Lakewood, CO.

[3.3] S. Guha, J. Yang, A. Banerjee, T. Glatfelter, K. Hoffman, S. R. Ovshinsky, M. Izu, H. C. Ovshinsky, and X. Deng, MRS Proc. **336**, 645, (1994).

[3.4] M. Izu, X. Deng, A. Krisko, K. Whelan, R. Young, H. C. Ovshinsky, K. L. Narasimhan, and S. R. Ovshinsky, 23rd IEEE PVSC, 919 (1993).

[3.5] E. A. DeMeo, Proc. of 10th EC Photovoltaic Solar Energy Conf., 1991, p1269.

[3.6] S. Guha, J. Yang, P. Nath, and M. Hack, Appl. Phys. Lett. 49, 218 (1986).

[3.7] B. von Roedern and G.H. Bauer, MRS Symposium Proc. 557 (1999).

[3.8] D.V. Tsu, B.s.Chao, S.R. Ovshinsky, S. Guha and J. Yang, App. Phys. Lett., 71, 1317 (1997).

[3.9] See. Review by Y.S. Tsuo and W. Luft, Appl. Phys. Comm, **10**, 71 (1990) and references there in.

[3.10] S. Guha, J.S. Payson, S.C. Agarwal and S.R. Ovshinsky, J. Non-Cryst. Solids **97-98**, 1455 (1988).

[3.11] J. Yang, R. Ross, T. Glatfelter, R. Mohr and S. Guha, MRS Poc. **149**, 435 (1989).

[3.12] A. Banerjee, X. Xu, J. Yang and S. Guha, MRS Proc. Vol. **377**, 675 (1995).

[3.13] X.B. Liao, J. Walker and X. Deng, MRS Symposium, April 1999.

[3.14] S.M. Sze , Physics of Semiconductor Devices, 2nd Edition, John Wiley & Sons, New York, 1981.

[3.15] J. Yang, A. Banerjee, and S. Guha, Appl. Phys. Lett., **70**, 2975 (1997).

[3.16] T. J. Coutts, N. M. Pearsall, and L. Tarricone, J. of Vac. Sci. & Tech., **B**, **2**, 140 (1984).

[3.17] S.S. Hegedus, W.A. Buchanan, E. Eser, J.E. Phillips, and W.N. Shafarman, AIP Conference Proceedings, Vol **394**, 547 (1997).

[3.18] X. Deng, G. Miller, G., R. Wang, L. Xu, and A.D. Compaan, 2nd world Conference on Photovoltaic Solar Energy Conversion, Vienna, Austria, 6-10 July 1998

4 Publications

4.1 Refereed papers published or in press (3/98-3/99):

1. A. Fischer, L. Anthony and A.D. Compaan, "Raman Analysis of Short-Range Clustering in Laser-Deposited CdS_xTe_{1-x} Films," Appl. Phys. Lett. **72**, 2559, (1998).
2. Y.L. Soo, S. Huang, Y.H. Kao, and A.D. Compaan, "Investigation of interface morphology and composition mixing in CdTe/CdS heterojunction photovoltaic materials using synchrotron radiation," J. Appl. Phys. **83**, 4173 (1998).
3. M. Tufino-Velazquez, G. Contreras-Puente, M.L. Albor-Aguilera, M.A. Gonzalez-Trujillo, and A.D. Compaan, "Thin Film Solar Cell Heterojunctions Deposited by rf Planar Magnetron Sputtering and HW-CVST," *Proc. of the 14th Photovoltaic Solar Energy Conference of Europe* (Barcelona, Spain-1997).
4. R. Wendt, A. Fischer, D. Grecu and A.D. Compaan, "Improvement of CdTe solar cell performance with discharge control during film deposition by magnetron sputtering," J. Appl. Phys. **84**, 2920-2925 (1998).
5. R. Wendt, A.D. Compaan, D. Grecu, K. Makhratchev, X. Ma, and R.G. Bohn, "CdTe Cell Performance vs. Plasma Parameters during Magnetron Sputter Deposition," 2nd World Conference and Exhibition on Photovoltaic Solar Energy Conversion--proceedings (Vienna, Austria, 6-10 July 1998, paper VD5.13, [report EUR 18656 EN by the Joint Research Centre European Commission, Luxembourg, 1998], pp. 1059-62.
6. X. Deng, G. Miller, R. Wang, L. Xu, and A.D. Compaan, "Study of Sputter Deposition of ITO Films for a-Si:H n-i-p Solar Cells," 2nd World Conference and Exhibition on Photovoltaic Solar Energy Conversion--proceedings (Vienna, Austria, 6-10 July, 1998, paper VB5.22).[report EUR 18656 EN by the Joint Research Centre European Commission, Luxembourg, 1998], pp. 700-703
7. S. Huang, Y.L. Soo, Y.H. Kao, and A.D. Compaan, "Annealing effects and Te mixing in CdTe/CdS heterojunctions," Appl. Phys. Lett., **74**, 218-220 (1999).
8. K. Wei, F.H. Pollak, J.L. Freeouf, D. Shvydka, and A.D. Compaan, "Optical Properties of $CdTe_{1-x}S_x$ ($0 \le x \le 1$): Experiment and Modeling," J. Appl. Phys. **85**, 7418-7425 (1999)
9. A.D. Compaan, I Matulionis, and S. Nakade, "Lasers and Beam Delivery Options for Polycrystalline Thin-Film Scribing," *NCPV Photovoltaics Program Review* (AIP Conference Proceedings No. 462, 1999 ed. by M. Al-Jassim, J.P.Thornton, and J.M. Gee), pp. 42-47.
10. D. Grecu and A.D. Compaan, "Photoluminescence Study of Cu Diffusion in CdTe," *NCPV Photovoltaics Program Review* (AIP Conference Proceedings No. 462, 1999 ed. by M. Al-Jassim, J.P. Thornton, and J.M. Gee), pp. 224-229.
11. X. Deng, "Study of Triple-Junction Amorphous Silicon Alloy Solar Cells", *NCPV Photovoltaics Program Review* (AIP Conference Proceedings No. 462, 1999 ed. by M. Al-Jassim, J.P. Thornton, and J.M. Gee), pp. 297-302.
12. D. Grecu and A.D. Compaan, "Photoluminescence Study of Cu Diffusion and Electromigration in CdTe, accepted for publication in Appl. Phys. Lett. (July, 1999).

4.2 Annual Subcontract Reports:

1. A.D. Compaan, Optimization of Laser Scribing for Thin-Film PV Modules, Annual Subcontract Report for the period 4/12/96-10/31/97, Contract No. ZAF-5-14142-08 [available from NTIS, publication NREL/SR-520-24842] (40 pages).
2. A.D. Compaan & R.G. Bohn, High Efficiency Thin-film Cadmium Telluride Photovoltaic Cells, Annual Subcontract Report for the period 1/21/97-3/31/98, Contract No. ZAX-4-14013 [available from NTIS, publication NREL/SR-520-25856] (41 pages).

4.3 Annual Reports published in NREL/SNL Annual Report, PV Subcontract Program:

1. A.D. Compaan, I. Matulionis and S. Nakade, "Optimization of Laser Scribing for Thin-film PV Modules," subcontract report published in: Annual Report, Photovoltaic Subcontract Program FY 1997, Contract No. ZAF-5-14142-08, [available from NTIS, publication NREL/BK-210-23607], pp. 317-320.
2. A.D. Compaan, R.G. Bohn, A. Fischer, R. Wendt, D. Grecu, E. Bykov, X. Deng, C. Narayanswamy, D. Zuo, X. Ma, and K. Makhratchev, "High Efficiency Thin-Film Cadmium Telluride Photovoltaic Cells," subcontract report published in: "Annual Report, Photovoltaic Subcontract Program, FY 1997, Contract No. ZAX-4-14013-4 [available from NTIS publication NREL/BK-210-23607], (pp. 321-324).

5 Project Personnel

5.1 Visiting professors/scientists

Xianbo Liao (from Institute of Semiconductors, Chinese Academy of Sciences) (5/98--)

5.2 Postdoctoral Associates:

Kent Price (Ph.D., U. of North Carolina, physics, 1998) (10/98--)
Sijin Han (Ph.D., U. of Science and Technology of China, 1998) (12/98--)

5.3 Graduate Students:

Ronghua Wang
M.S. completed May 1998: "Study of single-junction and triple-junction amorphous silicon based solar cells"

Greg Miller
M.S. completed August 1999: “Study of transparent conductive oxides in amorphous silicon based solar cells"

Shogo Nakade
M.S. completed Feb. 1999: "Time-Resolved Reflectivity Measurements on Thin-Film Photovoltaic Materials"

Chitra Narayanswamy
M.S. completed May 1999: "SIMS Analysis of Cu in ZnTe-Based Back Contacts for CdTe/CdS Solar Cells"

Xianda Ma
M.S. completed May 1999: "ZnTe:N Film as a Back Contact Material for Solar Cells"

Dan Grecu
M.S. completed 1998 (non thesis)
Ph.D. in progress

Ilvydas Matulionis
M.S. completed 1997 (non thesis)
Ph.D. in progress

Diana Shvydka
M.S. and Ph.D. in progress

Konstantin Makhratchev
M.S. and Ph.D. in progress

5.4 Undergraduate and high school students

5.4.1 NSF Research Experiences for Undergraduates *(REU)** (summer 1998)

Jennifer Drayton “Quantum Efficiency Studies of CdTe Solar Cells”

Ray Kallaher "Study of Indium Tin Oxide as the Top Contact in Hydrogenated Amorphous Silicon Based Solar Cells"

5.4.2 High School Summer Intern

Jonathan Smith “Cell Efficiency vs. CdTe thickness”

5.5 Technical Assistant: (1/95--8/95)

Robert Burmeister (4/96-) (25% time)

REPORT DOCUMENTATION PAGE

Form Approved
OMB NO. 0704-0188

1. AGENCY USE ONLY (Leave blank)	2. REPORT DATE	3. REPORT TYPE AND DATES COVERED
	December 1999	Annual Technical Report, 4 March 1998–3 March 1999

4. TITLE AND SUBTITLE
High-Efficiency Thin-Film CdTe and a-Si-Based Solar Cells; Annual Technical Report, 4 March 1998–3 March 1999

5. FUNDING NUMBERS
C: ZAF-8-17619-14
TA: PV005001

6. AUTHOR(S)
A.D. Compaan, X. Deng, and R.G. Bohn

7. PERFORMING ORGANIZATION NAME(S) AND ADDRESS(ES)
Department of Physics and Astronomy
University of Toledo
Toledo, OH 43606

8. PERFORMING ORGANIZATION REPORT NUMBER

9. SPONSORING/MONITORING AGENCY NAME(S) AND ADDRESS(ES)
National Renewable Energy Laboratory
1617 Cole Blvd.
Golden, CO 80401-3393

10. SPONSORING/MONITORING AGENCY REPORT NUMBER
SR-520-27666

11. SUPPLEMENTARY NOTES
NREL Technical Monitor: B. von Roedern

12a. DISTRIBUTION/AVAILABILITY STATEMENT
National Technical Information Service
U.S. Department of Commerce
5285 Port Royal Road
Springfield, VA 22161

12b. DISTRIBUTION CODE

13. ABSTRACT (Maximum 200 words)

This report describes work done by the University of Toledo during the first year of this subcontract. During this time, the CdTe group constructed a second dual magnetron sputter deposition facility; optimized reactive sputtering for ZnTe:N films to achieve 10 Ω-cm resistivity and ~9% efficiency cells with a copper-free ZnTe:N/Ni contact; identified Cu-related photoluminescence features and studied their correlation with cell performance including their dependence on temperature and E-fields; studied band-tail absorption in CdS_xTe_{1-x} films at 10 K and 300 K; collaborated with the National CdTe PV Team on 1) studies of high-resistivity tin oxide (HRT) layers from ITN Energy Systems, 2) fabrication of cells on the HRT layers with 0, 300, and 800-nm CdS, and 3) preparation of ZnTe:N-based contacts on First Solar materials for stress testing; and collaborated with Brooklyn College for ellipsometry studies of CdS_xTe_{1-x} alloy films, and with the University of Buffalo/Brookhaven NSLS for synchrotron X-ray fluorescence studies of interdiffusion in CdS/CdTe bilayers. The a-Si group established a baseline for fabricating a-Si-based solar cells with single, tandem, and triple-junction structures; fabricated a-Si/a-SiGe/a-SiGe triple-junction solar cells with an initial efficiency of 9.7% during the second quarter, and 10.6% during the fourth quarter (after 1166 hours of light-soaking under 1-sun light intensity at 50ºC, the 10.6% solar cells stabilized at about 9%); fabricated wide-bandgap a-Si top cells, the highest V_{oc} achieved for the single-junction top cell was 1.02 V, and top cells with high FF (up to 74%) were fabricated routinely; fabricated high-quality narrow-bandgap a-SiGe solar cells with 8.3% efficiency; found that bandgap-graded buffer layers improve the performance (V_{oc} and FF) of the narrow-bandgap a-SiGe bottom cells; and found that a small amount of oxygen partial pressure ($\sim 2 \times 10^{-5}$ torr) was beneficial for growing high-quality films from ITO targets.

14. SUBJECT TERMS
photovoltaics ; high efficiency ; CdTe ; a-Si ; thin films ; solar cells

15. NUMBER OF PAGES

16. PRICE CODE

17. SECURITY CLASSIFICATION OF REPORT	18. SECURITY CLASSIFICATION OF THIS PAGE	19. SECURITY CLASSIFICATION OF ABSTRACT	20. LIMITATION OF ABSTRACT
Unclassified	Unclassified	Unclassified	UL